# INVESTIGATION OF AN ELECTROOPTIC TUNABLE FILTER IN LITHIUM NIOBATE

A Dissertation

by

HSIN-HUI KUO

Submitted to the Office of Graduate Studies of
Texas A&M University
in partial fulfillment of the requirements for the degree of

DOCTOR OF PHILOSOPHY

May 2006

Major Subject: Electrical Engineering

# INVESTIGATION OF AN ELECTROOPTIC TUNABLE FILTER IN LITHIUM NIOBATE

A Dissertation

by

HSIN-HUI KUO

Submitted to the Office of Graduate Studies of
Texas A&M University
in partial fulfillment of the requirements for the degree of

DOCTOR OF PHILOSOPHY

Approved by :

| | |
|---|---|
| Chair of Committee, | Henry F. Taylor |
| Committee Members, | Ohannes Eknoyan |
| | Steven Wright |
| | Je-Chin Han |
| Head of Department, | Costas Georghiades |

May 2006

Major Subject: Electrical Engineering

# ABSTRACT

Investigation of an Electrooptic Tunable Filter in Lithium Niobate. (May 2006)

Hsin-Hui Kuo, B.S., National Tsing Hua University;

M.S., Columbia University

Chair of Advisory Committee: Dr. Henry F. Taylor

A polarization independent electrooptic add/drop tunable filter fabricated on a $LiNbO_3$ substrate with a narrow -3 dB bandwidth (FWHM) of 1.56 nm operating in the 1.55 μm wavelength regime has been developed to meet the demands of fast tuning speed and increased channel capacity for dense wavelength division multiplexed (WDM) networks. The operation of the filter is based on passive polarization beam splitters and strain-induced phase-matched TE↔TM polarization mode converters. Extinction ratios as high as 20 dB for polarization beam splitters were achieved using zero-gap two-mode interference directional couplers with an opening angle of 0.55°. A tunable TE↔TM polarization mode converter with 98.2 % conversion efficiency was obtained using a strain-induced refractive index grating consisting of 765 parallel strips 10.5 μm wide in a strained $SiO_2$ surface film with a spatial period of 21 μm. Thermal and electrooptic tuning of the polarization mode converters were examined. A polarization independent electrooptic add/drop tunable filter in which the fabrication parameters of the splitter and the mode converter were optimized was produced. Fiber-to-fiber insertion loss less than 6.3 dB was measured on a 62 mm long filter device. The spectral characteristics reveal a -3 dB bandwidth of 1.56 nm and nearest sidelobes about 12 dB below the center peak. A thermal tuning rate of -0.903 nm/°C was realized. Electrooptic tuning was also demonstrated. A tuning range of 14.08 nm with applied DC voltages from -80 V to +80 V was achieved indicating an electrooptic tuning rate of 0.086 nm/V. The filter performance for both TE and TM modes was examined and polarization independence of the spectral characteristics was confirmed.

To My Parents

# ACKNOWLEDGMENTS

I would like to thank my advisor and committee chair, Dr. H. F. Taylor, for his guidance and support through these years. And I would like to thank my committee member, Dr. O. Eknoyan, for his time, advice, and patience in every step of my research. Without them, this dissertation would not have been accomplished. I would also like to thank my committee member, Dr. J. C. Han, for his concern and encouragement during my study. I also appreciate the committee member, Dr. S. Wright, for his time and advice by serving as my committee member.

I truly appreciate Mr. R. A. Atkins and Mr. J. Gardner for their technical training and support in the lab. I also thank Ms. L. Huval for her help in many ways. I am very grateful to my friends and colleagues, N. Suphasan, A. Bhatranand, P. Tang, Y. Ping, R. Rebalo, R. Kim, Y. Shin, R. Wang, and D. Gu, for their friendship and support helping me through the toughest days.

I would like to thank Mrs. Han for her warm heartedness. As a close friend, she helped me throughout the days in College Station. I also thank my sisters for their love and understanding during these years. Finally I desire to give special thanks from the deepest of my heart to my parents for their love, support, encouragement, and always believing in me throughout ups and downs during my studies.

# TABLE OF CONTENTS

## TABLE OF CONTENTS (continued)

# TABLE OF CONTENTS (continued)

# LIST OF FIGURES

FIGURE Page

## LIST OF FIGURES (continued)

FIGURE Page

## LIST OF FIGURES (continued)

## LIST OF FIGURES (continued)

# LIST OF TABLES

# CHAPTER I

# INTRODUCTION

In recent years the use of personal computers and telecommunication networking has expanded tremendously. To support the increasing bandwidth demands of applications such as access to internet, World Wide Web browsing, and video conferencing, further advances in optical fiber networks are needed. A key attribute of the optical fiber is its large accessible spectral bandwidth. The bandwidth is around 30 THz between the transmission windows in the 1.3 μm and 1.5 μm spectral regimes in which most optical fiber networks operate. One way to exploit the huge bandwidth of an optical fiber is wavelength-division multiplexing (WDM) [1]. In WDM, the transmission spectrum of a single mode fiber is divided into non-overlapping communication channels. In present WDM networks the ability to route each individual wavelength is very limited, but dynamic wavelength routing is expected to be widely used in future network generations. Thus, high-speed devices will be required for packet- and cell-switched network in IP and asynchronous transfer mode (ATM) applications [2].

An optical tunable filter is a key device in dynamic WDM. From a system viewpoint, critical parameters of tunable filters are the number of accessible channels, the channel spacing, spectral tuning range, tuning speed, optical insertion loss, interchannel crosstalk, complexity, power consumption, and cost. The tuning range and

---

This dissertation follows the style and format of *IEEE Journal of Lightwave Technology*.

channel spacing determine the number of wavelength channels that can be used in the network. The tuning speed specifies the time needed to switch from one wavelength to another. Figure 1 shows the scheme of multi-channel spectrum of dynamic tuning [3]. The maximum number of channels is determined by the ratio of tuning range to channel spacing, and the bandwidth of the tunable filter is ~channel bandwidth B.

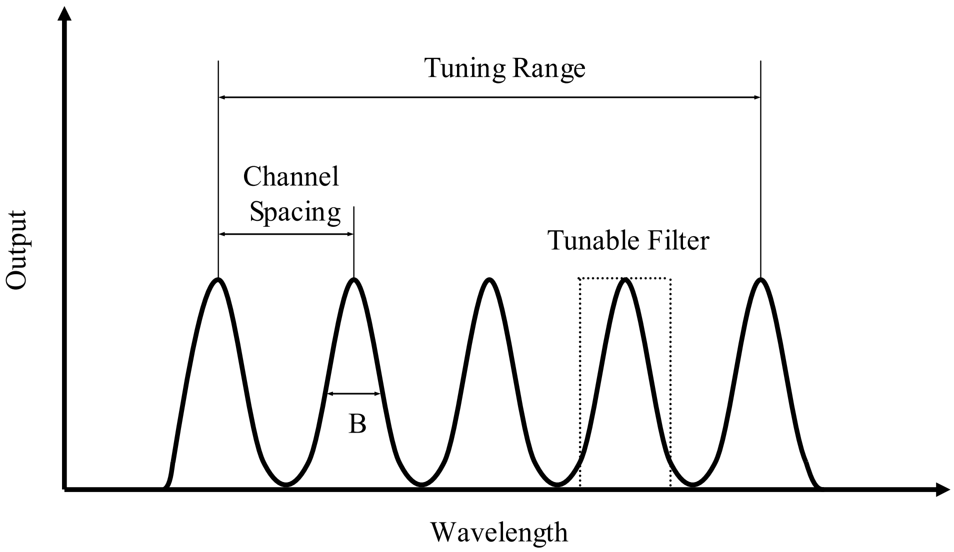

Figure 1. Multi-channel spectrum of a tunable filter.

Generally speaking, tunable filters can be divided into two main categories:

- Slow-speed tunable filters, with a few milliseconds tuning time, are used for circuit-switched networks. The tuning mechanism is mainly based on heat, thermo-optics, or piezo-electric (PZT) technologies, such as fiber Fabry-Perot interferometer (FFP), fiber Bragg grating (FBG), and arrayed waveguide grating (AWG) tunable filters [4-6].

- High-speed tunable filters, with microsecond and nanosecond tuning times, are used for packet- and cell- switched networks. The tuning mechanism is usually based on micro-machined, acousto-optic, or electro-optic, such as micromachined FP, cascaded Mach-Zehnder interferometer (MZI), acousto-optic, and electro-optic tunable filters (AOTF and EOTF) [7-10].

Most techniques and devices in the first category are already commercially available. However, in the high-speed category devices are in different research stages. The microsecond devices already had significant progress like acousto-optic tunable filters, whereas the nanosecond devices are still in the preliminary stage. Table 1 summaries the important characteristics of various reported technologies [11].

Table 1. Characteristics of various tunable filters.

| Filter Category | -3 dB Bandwidth | Tuning Range | Tuning Time |
|---|---|---|---|
| FFP | < 0.5 nm | ~ 10 nm | 1 ~ 10 ms |
| FBG | < 0.2 nm | < 10 nm | 1 ~ 10 ms |
| AWG | < 0.2 nm | ~ 40 nm | 10 ms |
| Micromachined FP | < 0.5 nm | ~ 60 nm | 100 μs |
| AOTF | ~ 1.5 nm | 250 nm | 10 μs |
| Cascaded MZI | < 0.2 nm | ~ 4 nm | 50 ns |
| EOTF | ~ 1.5 nm | ~ 16 nm | 1 ~ 10 ns |

At Texas A&M University the electro-optic tunable filter has been demonstrated with Ti-indiffused waveguides in a lithium niobate ($LiNbO_3$) substrate with a bandwidth of 2.3 nm [10].

The objective of this research is to develop a polarization independent electro-optic add/drop tunable filter in Ti:$LiNbO_3$ with a narrow bandwidth of 1.56 nm operating in the 1.55 μm wavelength regime, and input/output port separation suitable for optical fiber pigtailing.

# CHAPTER II

# THEORETICAL REVIEW

In this chapter optical wave propagation in dielectric waveguides and anisotropic crystals is treated, starting from Maxwell's equations. The electrooptic and photoelastic effects are presented. On the basis of coupled-mode theory, polarization mode conversion is explained.

## A. Wave Propagation

The electric and magnetic fields in a homogeneous, non-dispersive, and source-free medium satisfy the following partial differential equations, known as Maxwell's equations.

$$\nabla \times \mathbf{E} = -\frac{\partial \mathbf{B}}{\partial t} \tag{1}$$

$$\nabla \times \mathbf{H} = \frac{\partial \mathbf{D}}{\partial t} \tag{2}$$

$$\nabla \cdot \mathbf{D} = 0 \tag{3}$$

$$\nabla \cdot \mathbf{B} = 0 \tag{4}$$

where **E** (V/m) and **H** (A/m) represent electric and magnetic field vectors, **D** (C/m$^2$) is the electric flux density, and **B** (Wb/m$^2$) is the magnetic flux density.

The relation between **E** and **D** depends on the electric properties of the medium and similarly the relation between **H** and **B** depends on the magnetic properties of the medium. Two equations define these relations:

$$\mathbf{D} = \varepsilon_0 \mathbf{E} + \mathbf{P} = \varepsilon \mathbf{E} \tag{5}$$

$$\mathbf{B} = \mu_0 \mathbf{H} + \mu_0 \mathbf{M} \tag{6}$$

in which $\mathbf{P}$ (C/m$^2$) is the dielectric polarization density, $\mathbf{M}$ (A/m) is the magnetization density, $\varepsilon = \varepsilon_r \varepsilon_0$ where $\varepsilon$ (F/m) is the dielectric permittivity of the medium, $\varepsilon_0$ (F/m) is the dielectric permittivity of free space, and $\varepsilon_r$ is the relative permittivity (or dielectric constant). $\mu_0$ (H/m) is the magnetic permeability of free space and $\mathbf{M} = 0$ in a non-magnetic medium. In this research $\mathbf{B} = \mu_0 \mathbf{H}$.

Taking the curl of equation (1), substituting in equation (2) by employing equations (3), (4), (5), and (6), and using vector identity $\mathbf{A} \times \mathbf{B} \times \mathbf{C} = \mathbf{B}(\mathbf{A} \cdot \mathbf{C}) - \mathbf{C}(\mathbf{A} \cdot \mathbf{B})$ gives us the wave equation

$$\nabla^2 \mathbf{E} - \varepsilon \mu_0 \frac{\partial^2 \mathbf{E}}{\partial t^2} = 0 . \tag{7}$$

When the electromagnetic wave is monochromatic, all components of electric and magnetic fields are harmonic functions of time. The electric field vector $\mathbf{E}$ is given by

$$\mathbf{E}(\mathbf{r}, t) = \mathbf{E}(\mathbf{r}) e^{jwt} . \tag{8}$$

Substituting equation (8) into (7), equation (7) becomes

$$\nabla^2 \mathbf{E}(\mathbf{r}) + n^2 k_0^2 \mathbf{E}(\mathbf{r}) = 0 \tag{9}$$

where $k_0 = \frac{w}{c}$ is the propagation constant in free space, $c = \frac{1}{\sqrt{\mu_0 \varepsilon_0}}$ is the light speed in free space, and $n = \sqrt{\varepsilon_r}$ is the refractive index of the medium.

### B. Optical Waveguides

Light can be guided within a high refractive index region surrounded by lower refractive index material through total internal reflection (TIR). A simple planar waveguide shown in Figure 2 is introduced to explain wave propagation. At the boundary between two dielectric media the tangential components of electric field **E** and magnetic field **H**, and the normal components of electric flux density **D** and magnetic flux density **B** should be continuous.

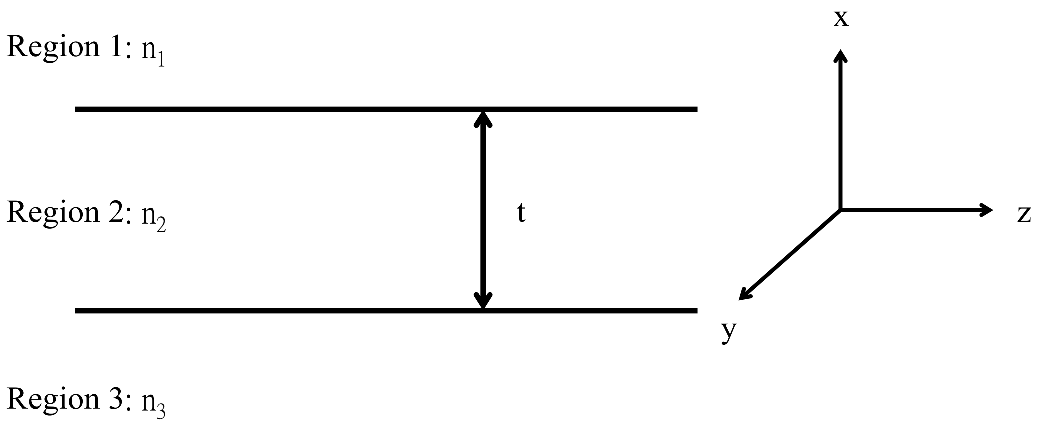

Figure 2. Planar dielectric waveguide.

In a planar waveguide the wave propagates along z-direction with propagation constant $\beta$, and electric field vector **E** can be taken as

$$\mathbf{E}(\mathbf{r},t) = \mathbf{E}(x,y)e^{j(wt-\beta z)}. \tag{10}$$

Since there is no variation along y-direction in the planar waveguide, $\partial / \partial y = 0$. Applying this and equation (10) in equation (9), the results for the three regions yield [12]

$$\begin{aligned}
&\text{Region } 1: \ \frac{d^2}{dx^2}\mathrm{E}(x) + (k_0^2 n_1^2 - \beta^2)\mathrm{E}(x) = 0 \\
&\text{Region } 2: \ \frac{d^2}{dx^2}\mathrm{E}(x) + (k_0^2 n_2^2 - \beta^2)\mathrm{E}(x) = 0 \qquad (11) \\
&\text{Region } 3: \ \frac{d^2}{dx^2}\mathrm{E}(x) + (k_0^2 n_3^2 - \beta^2)\mathrm{E}(x) = 0
\end{aligned}$$

where E(x) is a Cartesian component of **E**(x).

Assuming $\mathrm{n}_2 > \mathrm{n}_3 > \mathrm{n}_1$, the characteristics of waveguide modes can be analyzed by various values of the waveguide propagation constant $\beta$. For $\beta < k_0 n_1$, the solutions of E(x) in equation (11) are sinusoidal in all three regions. These are radiation modes and the lightwave is not guided. For $k_0 n_1 < \beta < k_0 n_3$, the solutions of E(x) correspond to exponential behavior in region 1 and sinusoidal behavior in region 2 and 3. This is referred as the substrate radiation mode. For $k_0 n_3 < \beta < k_0 n_2$, the solutions of E(x) show exponential decay in region 1 and 3, and sinusoidal in region 2. This makes the propagating wave possible to satisfy the boundary conditions mentioned earlier. In this case, the optical wave is confined within the middle layer (region 2) and these are considered as guided modes. For $\beta > k_0 n_2$, the solutions of E(x) are exponential in all three regions. Because the field increases without bound away from the waveguide, the solution is not physically realizable. The electric field distributions of the above cases are illustrated in Figure 3.

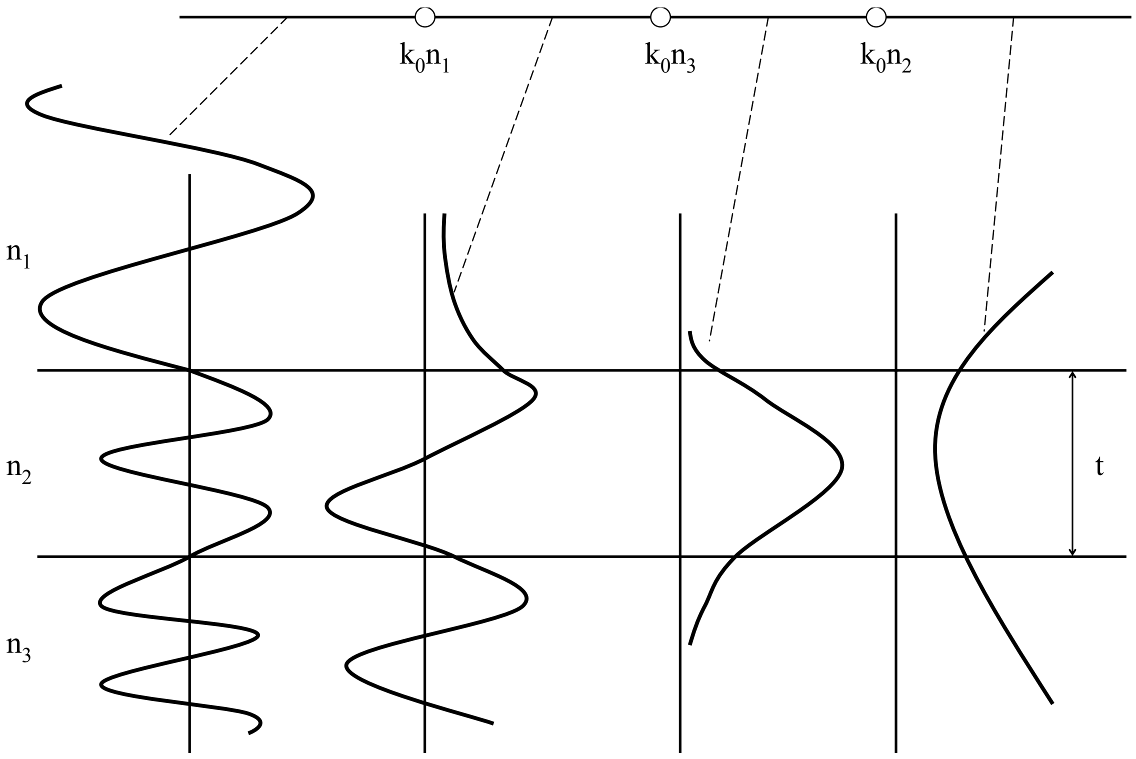

Figure 3. Electric field distributions of the planar waveguide corresponding to different values of the propagation constant $\beta$ with $n_2 > n_3 > n_1$.

From the above analysis, the condition to have confined propagation modes in a waveguide is $k_0 n_3 < \beta < k_0 n_2$ with discrete values of $\beta$. The middle layer must have the higher refractive index than the surrounding media, i.e., $n_2 > n_3, n_1$.

The planar waveguide shown in Figure 2 can support a finite number of guided modes depending on the thickness t of the middle layer and the value of $\beta$. These modes can be divided into two groups corresponding to two orthogonal polarization states. One is transverse electric (TE) mode with the electric field polarized in y-direction. The field components of TE mode are $E_y$, $H_x$, and $H_z$. The other is transverse magnetic (TM) mode with the magnetic field polarized in y-direction. The field components of TM mode are $H_y$, $E_x$, and $E_z$. In practical application, the waveguide must be able to support at least the lowest order mode called the fundamental mode, and the waveguide supporting only the fundamental mode is a single mode waveguide.

### C. Optical Indicatrix in Uniaxial Crystals

In isotropic media, the relation between polarization density **P** and electric field **E** is independent of the direction of the field vector **E** so that the medium looks the same from all directions. The vectors **P** and **E** are parallel to each other.

$$\mathbf{P} = \varepsilon_0 \chi \mathbf{E} \tag{12}$$

where $\chi$ is a scalar constant called the electric susceptibility. However, in the case of anisotropic media the relation between vectors **P** and **E** does depend on the direction of electric field vector **E**, and the electric susceptibility $\chi$ is no longer a constant.

$$\mathbf{P} = \varepsilon_0 \tilde{\chi} \mathbf{E} \tag{13}$$

where $\tilde{\chi}$ is a $3 \times 3$ array known as the susceptibility tensor.

Applying equation (13) into (5), the relation between the electric flux density vector **D** and the electric field vector **E** becomes

$$\mathbf{D} = \tilde{\varepsilon} \mathbf{E} \tag{14}$$

where $\tilde{\varepsilon}$ is a $3 \times 3$ array called the dielectric permittivity tensor. To simplify the analysis the orthogonal coordinate axes are transformed to the principal axes so that all off-diagonal components of the tensor $\tilde{\varepsilon}$ are zero.

$$\tilde{\varepsilon} = \begin{pmatrix} \varepsilon_{11} & 0 & 0 \\ 0 & \varepsilon_{22} & 0 \\ 0 & 0 & \varepsilon_{33} \end{pmatrix} = \varepsilon_0 \begin{pmatrix} n_1^2 & 0 & 0 \\ 0 & n_2^2 & 0 \\ 0 & 0 & n_3^2 \end{pmatrix} \tag{15}$$

where $\varepsilon_{11}, \varepsilon_{22}$, and $\varepsilon_{33}$ are principal permittivities.

The stored electric energy density in the crystal is

$$U_e = \frac{1}{2}\mathbf{E}\cdot\mathbf{D}. \tag{16}$$

Substituting equations (14) and (15) into equation (16),

$$U_e = \frac{1}{2}\left[\frac{D_x^2}{\varepsilon_{11}} + \frac{D_y^2}{\varepsilon_{22}} + \frac{D_z^2}{\varepsilon_{33}}\right]. \tag{17}$$

Replacing $\frac{D_i}{\sqrt{2\varepsilon_0 U_e}}$ with $i$, where $i =$x, y, z, equation (17) is abbreviated by

$$\frac{x^2}{n_x^2} + \frac{y^2}{n_y^2} + \frac{z^2}{n_z^2} = 1. \tag{18}$$

Equation (18) represents the index ellipsoid or indicatrix with principal axes x, y, and z [13].

Optical properties of a crystal are determined by its crystal structure. For uniaxial crystals the index ellipsoid is rotationary symmetric with respect to z-axis, also known as optic axis, and $n_x = n_y \neq n_z$ such as $LiNbO_3$ and $LiTaO_3$; $n_x = n_y \equiv n_o$ and $n_z \equiv n_e$ where $n_o$ and $n_e$ are referred to ordinary and extraordinary refractive indices, respectively. Figure 4 shows the index ellipsoid of an uniaxial crystal.

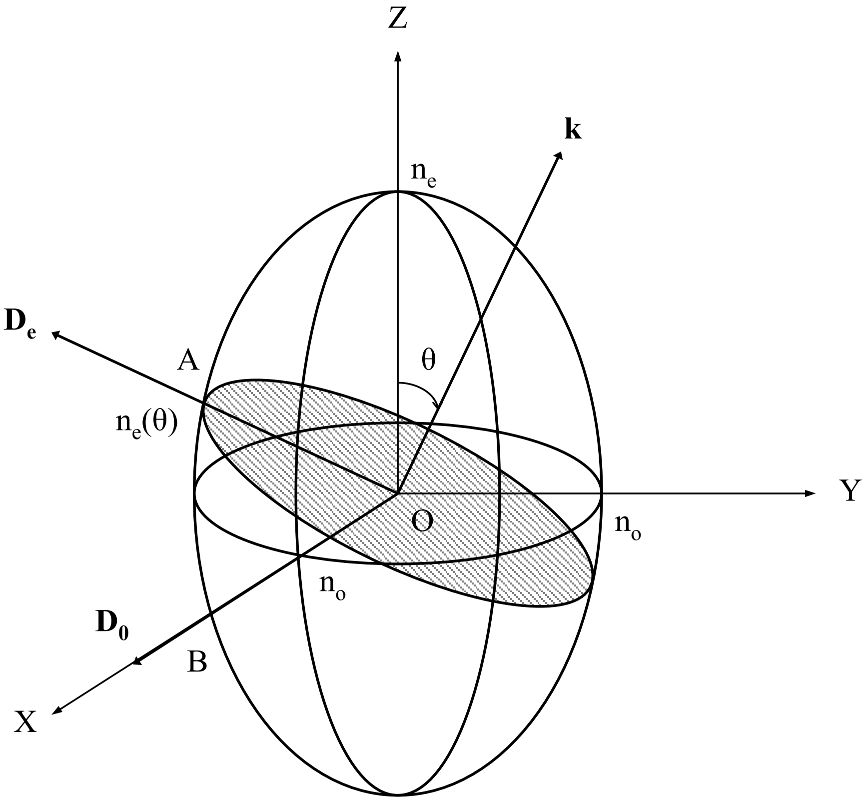

Figure 4. The index ellipsoid of an uniaxial crystal.

Considering light propagation in an uniaxial crystal **k** denotes an arbitrary propagating lightwave having an angle θ with respect to z-axis. Because of the rotational symmetry around z-axis, the projection of the vector **k** on the x-y plane is chosen to coincide with the y-axis without loss of generality. The intersection ellipse normal to the propagation vector **k** is shaded in Figure 4. Two orthogonal linear-polarized lightwaves exist for the propagating lightwave. One is referred to as ordinary wave polarized along OB direction and it sees the refractive index $n_o$ regardless of the incident angle θ. The other is called extraordinary wave polarized along OA direction and it sees the refractive index $\mathrm{n_e}(\theta)$, thus depends on the propagation direction. The existence of these two linearly polarized waves, ordinary and extraordinary, causes the birefringence in the crystal. The length of OA, $\mathrm{n_e}(\theta)$, is given by

$$\begin{aligned} n_e^2(\theta) &= y^2 + z^2 \\ y &= n_e(\theta)\cos\theta \ . \\ z &= n_e(\theta)\sin\theta \end{aligned} \tag{19}$$

Substituting equation (19) into (18), gives

$$n_e(\theta) = \frac{n_e n_o}{\sqrt{n_e^2 \cos^2\theta + n_o^2 \sin^2\theta}} \ . \tag{20}$$

Equation (20) shows that the refractive index of the extraordinary wave varies from $\mathrm{n_e}(0^\circ) = \mathrm{n_o}$ to $\mathrm{n_e}(90^\circ) = \mathrm{n_e}$. Particularly when $\theta = 0^\circ$, the crystal will act as optically isotropic.

## D. Electrooptic Effect

In the following sections D and E, optical waves propagation in a crystal in the presence of an applied electric field or a mechanical strain will be discussed. In section C we found given an arbitrary propagating wave in an uniaxial crystal two orthogonal linear-polarized waves exist. The ordinary and extraordinary refractive indices can be changed with an applied electric field. This is known as the electrooptic effect. The linear relation between the refractive index and the applied electric field is called Pockels effect, and the quadratic relation between the refractive index and the electric field is called Kerr effect. Since the Pockels effect is commonly used in integrated optics and also induces larger refractive index changes, the discussion here is focused on Pockels effect. Pockels effect occurs only in crystals without inversion symmetry, so the sign of the index change depends on the polarity of the voltage applied to the crystal. Electrooptically induced index changes can be characterized by specifying changes in the index ellipsoid equation (18). In the presence of an applied electric field, the index ellipsoid equation is expressed by

$$\left(\frac{1}{n^2}\right)_1 x^2+\left(\frac{1}{n^2}\right)_2 y^2+\left(\frac{1}{n^2}\right)_3 z^2+2\left(\frac{1}{n^2}\right)_4 yz+2\left(\frac{1}{n^2}\right)_5 xz+2\left(\frac{1}{n^2}\right)_6 xy=1\,. \qquad (21)$$

If x, y, and z are chosen to be parallel to the crystal principal axes without an applied electric field, equation (21) will reduce to equation (18). Therefore

$$\left.\left(\frac{1}{n^2}\right)_i\right|_{E=0}=\begin{cases}\dfrac{1}{n_j^2}, i=1,2,3\\ 0\ , i=4,5,6\end{cases} \qquad (22)$$

where j = 1, 2, 3 denotes x, y, z, respectively. With the presence of an electric field, the inverse of indices in equation (21) are expressed as

$$\left.\left(\frac{1}{n^2}\right)_i\right|_{E\neq 0}=\begin{cases}\dfrac{1}{n_j^2}+\Delta\left(\dfrac{1}{n^2}\right)_i\ , i=1,2,3\\ 0+\Delta\left(\dfrac{1}{n^2}\right)_i\ , i=4,5,6\end{cases}. \qquad (23)$$

The induced refractive index change $\Delta\left(\frac{1}{n^2}\right)_i$ due to an applied electric field is defined by

$$\Delta\left(\frac{1}{n^2}\right)_i=\sum_{j=1}^{3} r_{ij}E_j \qquad (24)$$

where i=1, 2, …, 6. $E_j$ is the component of the applied electric field, and $r_{ij}$ is a $6\times 3$ electrooptic coefficient tensor. In a LiNbO3 crystal, $n_x = n_y = n_o$ and $n_z = n_e$, the electrooptic tensor is [13]

$$\begin{pmatrix} 0 & -r_{22} & r_{13} \\ 0 & r_{22} & r_{13} \\ 0 & 0 & r_{33} \\ 0 & r_{51} & 0 \\ r_{51} & 0 & 0 \\ -r_{22} & 0 & 0 \end{pmatrix} \tag{25}$$

where $r_{33} = 30.8\times 10^{-12}$ m/V, $r_{13} = 8.6\times 10^{-12}$ m/V, $r_{22} = 3.4\times 10^{-12}$ m/V, and $r_{51} = 26\times 10^{-12}$ m/V.

Assuming the applied electric field **E** is along the z-direction of a LiNbO3 crystal, with equations (21), (24), and (25) the index ellipsoid equation becomes

$$\left(\frac{1}{n_o^2} + r_{13}E_z\right)x^2 + \left(\frac{1}{n_o^2} + r_{13}E_z\right)y^2 + \left(\frac{1}{n_e^2} + r_{33}E_z\right)z^2 = 1. \tag{26}$$

According to equation (26), new refractive indices with principal axes can be found as

$$\begin{aligned} \frac{1}{n_x^2} &= \frac{1}{n_o^2} + r_{13}E_z \\ \frac{1}{n_y^2} &= \frac{1}{n_o^2} + r_{13}E_z \,. \\ \frac{1}{n_z^2} &= \frac{1}{n_e^2} + r_{33}E_z \end{aligned} \tag{27}$$

Since the electrooptic coefficients are very small, then $n_o^2 r_{13} E_z << 1$ and $n_e^2 r_{33} E_z << 1$. Therefore $(1+x)^a \approx 1 + ax$ can applied, and new refractive indices obtained as

$$\begin{aligned} n_x &= n_o - \frac{1}{2} n_o^3 r_{13} E_z \\ n_y &= n_o - \frac{1}{2} n_o^3 r_{13} E_z \ . \\ n_z &= n_e - \frac{1}{2} n_e^3 r_{33} E_z \end{aligned} \tag{28}$$

In case the applied electric field is not parallel to the z-direction, there will be mixed terms showing in the index ellipsoid equation (21). The major axes of the ellipsoid are no longer corresponding to the principal axes (x, y, and z), and due to the rotation of new principal axes of index ellipsoid the new refractive indices need to be recalculated.

## E. Photoelastic Effect

The photoelastic effect couples the mechanical strain to the optical refractive index and induces index changes. This effect can be described in the same manner as the linear electrooptic effect shown in equation (24) as [12]

$$\Delta\left(\frac{1}{n^2}\right)_{ij} = P_{ijkl} S_{kl} \tag{29}$$

where i, j, k, l = 1, 2, 3 and $\left(\frac{1}{\mathrm{n}^2}\right)_{\mathrm{ij}}$ is the constant of the index ellipsoid equation (21). $\mathrm{P}_{\mathrm{ijkl}}$ is the photoelastic fourth-order tensor [14], and $\mathrm{S}_{\mathrm{kl}}$ is the strain component defined as

$$S_{kl}(\mathbf{r}) = \frac{1}{2}\left[\frac{\partial u_k(\mathbf{r})}{\partial x_l} + \frac{\partial u_l(\mathbf{r})}{\partial x_k}\right] \tag{30}$$

where $\mathrm{u_k}(\mathbf{r})$ is the displacement of a point **r** in the crystal projected along the direction k.

To find out the relation between $\Delta\left(\frac{1}{n^2}\right)_{ij}$ and the dielectric tensor $\tilde{\varepsilon}$, equation (14) becomes

$$E_i = g_{ij} D_j \tag{31}$$

where $\tilde{\mathrm{g}} = (\tilde{\varepsilon})^{-1}$ is the inverse of the matrix $\tilde{\varepsilon}$. Because of $\varepsilon_{\mathrm{ij}} << \varepsilon_{\mathrm{ii}} (\mathrm{i} \neq \mathrm{j})$, the rule of matrix inversion is applied.

$$\begin{aligned} g_{ii} &= (\varepsilon_{ii})^{-1} \\ g_{ij,\, i\neq j} &\cong -\frac{\varepsilon_{ji}}{\varepsilon_{ii}\varepsilon_{jj}} = -\frac{\varepsilon_{ij}}{\varepsilon_{ii}\varepsilon_{jj}}. \end{aligned} \tag{32}$$

Using equations (31), (32) and defining $\varepsilon'_{ij} = \frac{\varepsilon_{ij}}{\varepsilon_0}$, equation (16) results in

$$2U_e\varepsilon_0 = \frac{D_x^2}{\varepsilon'_{11}} + \frac{D_y^2}{\varepsilon'_{22}} + \frac{D_z^2}{\varepsilon'_{33}} - 2\frac{\varepsilon'_{32}}{\varepsilon'_{33}\varepsilon'_{22}} D_z D_y - 2\frac{\varepsilon'_{31}}{\varepsilon'_{33}\varepsilon'_{11}} D_z D_x - 2\frac{\varepsilon'_{21}}{\varepsilon'_{22}\varepsilon'_{11}} D_y D_x. \tag{33}$$

Replacing $\mathbf{D} = \sqrt{2\varepsilon_0 \mathrm{U_e}}\,\mathbf{r}$, where **r** = (x, y, z), equation (33) yields

$$\frac{x^2}{\varepsilon'_{11}} + \frac{y^2}{\varepsilon'_{22}} + \frac{z^2}{\varepsilon'_{33}} - 2\frac{\varepsilon'_{32}}{\varepsilon'_{33}\varepsilon'_{22}} zy - 2\frac{\varepsilon'_{31}}{\varepsilon'_{33}\varepsilon'_{11}} zx - 2\frac{\varepsilon'_{21}}{\varepsilon'_{22}\varepsilon'_{11}} yx = 1. \tag{34}$$

This is the index ellipsoid equation. The constant of each term in equation (34) can be defined as

$$\begin{cases} \left(\dfrac{1}{n^2}\right)_{ii} = \dfrac{1}{\varepsilon'_{ii}} \\ \left(\dfrac{1}{n^2}\right)_{ij,i\neq j} = -\dfrac{\varepsilon'_{ij}}{\varepsilon'_{ii}\varepsilon'_{jj}} \end{cases} \tag{35}$$

with i, j = 1, 2, 3. Using equation (35), equation (29) can be expressed as

$$\Delta\varepsilon'_{ij} = -\varepsilon'_{ii}\varepsilon'_{jj}P_{ijkl}S_{kl}\,. \tag{36}$$

As mentioned in section A, $\varepsilon'_{ii}$ is equal to $n_{ii}^2$ for the diagonal components, and $\Delta\varepsilon'_{ii} = 2n_{ii}\Delta n_{ii}$ can be derived. Extending this to the off-diagonal components leads to

$$\Delta n_{ij} = \frac{1}{2}(n_{ii}n_{jj})^{-\frac{1}{2}}\Delta\varepsilon'_{ij}\,. \tag{37}$$

Substituting equation (36) into (37), it becomes

$$\Delta n_{ij} = -\frac{1}{2}\sqrt{n_{ii}^3 n_{jj}^3}\,P_{ijkl}S_{kl}\,. \tag{38}$$

The strain tensor $S_{kl}$ and the photoelastic tensor $P_{ijkl}$ can be expressed as a six-component vector and a second-order tensor having $6\times6$ components, respectively by correlating α = 1, 2, 3, 4, 5, 6 to ij = 11, 22, 33, 23, 31, 12 and β = 1, 2, 3, 4, 5, 6 to kl = 11, 22, 33, 23, 31, 12. Therefore, equation (38) yields

$$\Delta n_{\alpha} = -\frac{1}{2}n_{\alpha}^3 P_{\alpha\beta}S_{\beta} \tag{39}$$

where $n_\alpha = \sqrt{n_{ii}n_{jj}}$, $P_{\alpha\beta} = P_{ijkl}$, and $S_\beta = S_{kl}$. Based on the definition of equation (30), the six-component vector $S_\beta$ is given by [15]

$$\begin{pmatrix} S_1 \\ S_2 \\ S_3 \\ S_4 \\ S_5 \\ S_6 \end{pmatrix} = \begin{pmatrix} \dfrac{\partial u_1}{\partial x_1} \\ \dfrac{\partial u_2}{\partial x_2} \\ \dfrac{\partial u_3}{\partial x_3} \\ \dfrac{1}{2}\left(\dfrac{\partial u_2}{\partial x_3} + \dfrac{\partial u_3}{\partial x_2}\right) \\ \dfrac{1}{2}\left(\dfrac{\partial u_1}{\partial x_3} + \dfrac{\partial u_3}{\partial x_1}\right) \\ \dfrac{1}{2}\left(\dfrac{\partial u_1}{\partial x_2} + \dfrac{\partial u_2}{\partial x_1}\right) \end{pmatrix} \tag{40}$$

where 1, 2, and 3 indicate x, y, and z, respectively. $S_1$, $S_2$, and $S_3$ are longitudinal strain components and $S_4$, $S_5$, and $S_6$ are shear strain components.

### F. TE $\leftrightarrow$ TM Mode Conversion

By means of a refractive index perturbation in a waveguide, TE-polarized input light can be converted into TM-polarized output light and vice versa. The basic idea of TE $\leftrightarrow$ TM conversion can be described by a small perturbation of the dielectric polarization density **P**, and examining this perturbation effect with the time dependent wave equation. The wave equation in a dielectric medium is

$$\nabla^2 \mathbf{E}(\mathbf{r},t) = \varepsilon(\mathbf{r})\mu_0 \frac{\partial^2 \mathbf{E}(\mathbf{r},t)}{\partial t^2}. \tag{41}$$

Substituting equation (5) into (41), yields

$$\nabla^2 \mathbf{E}(\mathbf{r},t) = \varepsilon_0\mu_0 \frac{\partial^2 \mathbf{E}(\mathbf{r},t)}{\partial t^2} + \mu_0 \frac{\partial^2 \mathbf{P}(\mathbf{r},t)}{\partial t^2}. \tag{42}$$

Assuming the wave propagates through a perturbed medium with index gratings, the dielectric polarization **P** can be considered as the sum of two terms, unperturbed and perturbed polarizations,

$$\mathbf{P}(\mathbf{r},t) = \mathbf{P}_o(\mathbf{r},t) + \mathbf{P}_{pert}(\mathbf{r},t) \tag{43}$$

with

$$\mathbf{P}_o(\mathbf{r},t) = \left[\varepsilon(\mathbf{r}) - \varepsilon_0\right]\mathbf{E}(\mathbf{r},t). \tag{44}$$

Using equations (43) and (44), equation (42) becomes

$$\nabla^2 E_i(\mathbf{r},t) - \mu_0 \varepsilon(\mathbf{r}) \frac{\partial^2 E_i(\mathbf{r},t)}{\partial t^2} = \mu_0 \frac{\partial^2}{\partial t^2}\left[\mathbf{P}_{pert}(\mathbf{r},t)\right]_i \tag{45}$$

where i indicates x, y, or z and $\mathrm{E_i}(\mathbf{r},\mathrm{t})$ is a component of $\mathbf{E}(\mathbf{r},\mathrm{t})$.

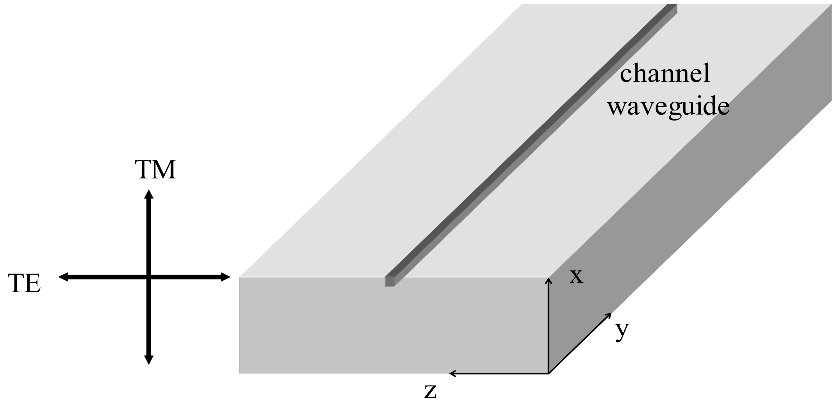

Figure 5. Polarization directions of TE and TM modes propagation along y-direction in an optical channel waveguide on an x-cut substrate.

In an x-cut y-propagating channel waveguide as shown in Figure 5, the TE-polarized wave has its transverse electric field along z-direction ($\mathrm{E_x} = 0$, $\mathrm{E_z} \neq 0$) while the TM-polarized wave has its transverse electric field along x-direction ($\mathrm{E_z} = 0$, $\mathrm{E_x} \neq 0$). Equation (45) shows that to achieve coupling from a TE-mode into a TM-mode, an x-directed induced perturbation polarization $\mathrm{P_x}$ is needed while for coupling a TM-mode into a TE-mode, a z-directed induced perturbation polarization $\mathrm{P_z}$ is required. Based on equation (5),

$$D_i = \varepsilon_{ij} E_j = \varepsilon_0 E_i + P_i \,. \tag{46}$$

The solution to the polarization $\mathrm{P_i}$ is

$$P_i = (\varepsilon_{ij} - \varepsilon_0 \delta_{ij}) E_j \,. \tag{47}$$

Thus, the perturbation of medium polarization $\mathrm{P_{pert}}$ can be expressed as

$$\left[ P_{pert} \right]_i = \Delta P_i = \Delta\varepsilon_{ij} E_j = \varepsilon_0 (\Delta\varepsilon'_{ij}) E_j \,. \tag{48}$$

Applying equations (29) and (36) into equation (48), $\mathrm{P_{pert}}$ yields

$$\left[ P_{pert} \right]_i = \Delta P_i = -\varepsilon_0 \varepsilon'_{ii} \varepsilon'_{jj} \Delta \left( \frac{1}{n^2} \right)_{ij} E_j \,. \tag{49}$$

Based on the above analysis, two cases are considered here. First TE$\rightarrow$TM mode conversion occurs with TE-polarized input along z-direction indicated as 3. In equation (49) the perturbation polarization $\Delta\mathrm{P_x}$ along x-direction indicated as 1 is

$$\Delta P_1 = -\varepsilon_0 \varepsilon'_{11} \varepsilon'_{33} \Delta \left( \frac{1}{n^2} \right)_{13} E_3 \tag{50}$$

where $\varepsilon'_{11} = n_o^2$ and $\varepsilon'_{33} = n_e^2$. Using reduced notation, equation (50) becomes

$$\Delta P_1 = -\varepsilon_0 n_o^2 n_e^2 \Delta\left(\frac{1}{n^2}\right)_5 E_3 . \tag{51}$$

Second case is TM$\rightarrow$TE mode conversion with TM-polarized input along x-direction. Following the same argument the perturbation polarization $\Delta \mathrm{P_z}$ along z-direction is

$$\Delta P_3 = -\varepsilon_0 n_o^2 n_e^2 \Delta\left(\frac{1}{n^2}\right)_5 E_1 . \tag{52}$$

Equations (51) and (52) show that TE$\leftrightarrow$TM mode conversion can be realized through the induced refractive index change $\Delta \mathrm{n}_5$ via the photoelastic effect.

Based on coupled-mode theory [12] TE$\leftrightarrow$TM mode conversion can be analyzed. The following equations describe the coupling relation between these two orthogonal modes.

$$\begin{cases} \dfrac{dA_m(y)}{dy} = -j\kappa B_m(y) e^{-j(\beta_m^{TM} - \beta_m^{TE})y} \\ \dfrac{dB_m(y)}{dy} = -j\kappa A_m(y) e^{+j(\beta_m^{TM} - \beta_m^{TE})y} \end{cases} \tag{53}$$

where $\mathrm{A_m}$ and $\mathrm{B_m}$ are the amplitudes of TE and TM m<sup>th</sup> mode; $\beta_\mathrm{m}^{\mathrm{TE}}$ and $\beta_\mathrm{m}^{\mathrm{TM}}$ are the propagating constants of TE and TM m<sup>th</sup> mode; κ is the coupling coefficient, and y is the propagation direction. The solutions to equation (53) with the initial conditions $\mathrm{B_m(y=0)=B_0}$ and $\mathrm{A_m(y=0)=0}$ are

$$\begin{cases} A_m(y) = aB_0 e^{-j\delta y} \\ B_m(y) = bB_0 e^{+j\delta y} \end{cases} \tag{54}$$

where

$$a = -j\frac{\kappa}{(\kappa^2+\delta^2)^{1/2}}\sin\left[(\kappa^2+\delta^2)^{1/2}y\right]$$

$$b = \cos\left[(\kappa^2+\delta^2)^{1/2}y\right] - j\frac{\delta}{(\kappa^2+\delta^2)^{1/2}}\sin\left[(\kappa^2+\delta^2)^{1/2}y\right]. \tag{55}$$

$$\delta = \frac{1}{2}(\beta_m^{TM} - \beta_m^{TE})$$

A plot of TE and TM mode power exchange normalized to input intensity $|B_0|^2$ is shown in Figure 6. With the phase-matched condition $\delta = 0$, TE and TM modes are coupled into each other completely, whereas with $\delta \neq 0$ only partial power exchange happens because of phase mismatch between TE and TM modes and δ is called the phase-mismatch factor.

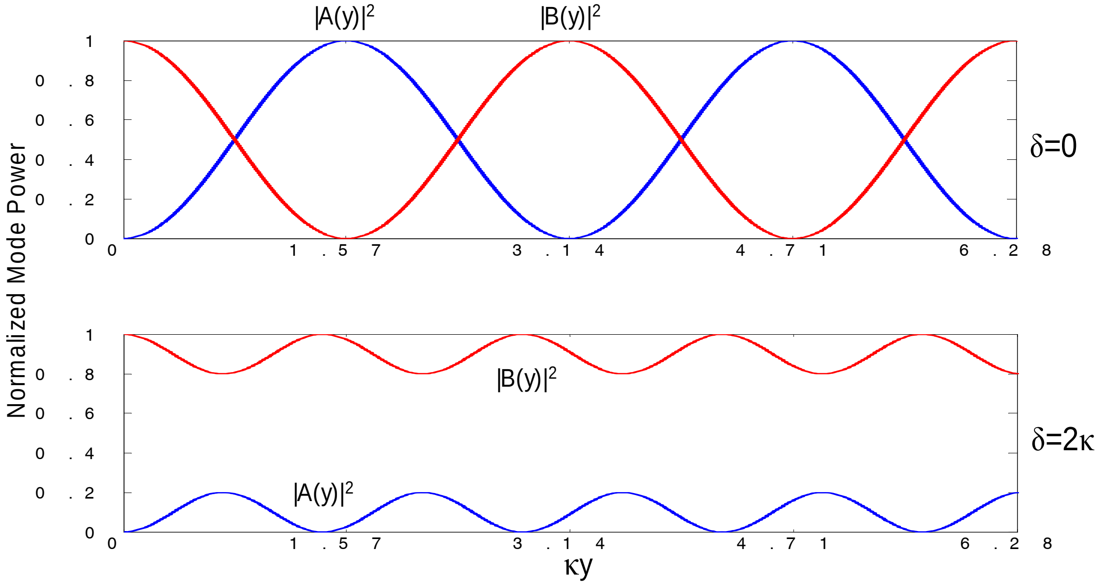

Figure 6. Power exchange between TE and TM modes with δ=0 and δ=2κ.

Since $\beta_{TM} = \frac{2\pi}{\lambda_o} n_o$, $\beta_{TE} = \frac{2\pi}{\lambda_o} n_e$, and $n_o \neq n_e$, practically the phase-mismatch factor $\delta \neq 0$. A deliberate period variation with a period $\Lambda$ is introduced to neutralize this phase mismatch and the phase-mismatch factor $\delta$ can be described as [16]

$$\delta = \frac{\beta_{TM} - \beta_{TE}}{2} - \frac{\pi}{\Lambda}. \tag{56}$$

To satisfy the phase-matched condition, $\delta = 0$,

$$\Lambda = \frac{2\pi}{|\beta_{TM} - \beta_{TE}|} = \frac{2\pi}{(2\pi/\lambda_o)|n_{TM} - n_{TE}|} = \frac{\lambda_o}{|n_{TM} - n_{TE}|}. \tag{57}$$

Since the period $\Lambda$ is a fixed value, according to the result shown in equation (57) the coupling between TE and TM modes is highly wavelength selective and the selected wavelength $\lambda_o$ can be tuned by changing the birefringence $|n_{TM}\text{-}n_{TE}|$.

# CHAPTER III

# DEVICE STRUCTURE AND ANALYSIS

In this chapter the structure of a tunable add/drop filter is presented, and its overall principle of operation is explained. The design and properties of each individual component required to form an integrated optical tunable filter are discussed.

## A. Filter Structure and Principle of Operation

The structure of an integrated optical add/drop tunable filter formed by Ti-indiffused waveguides on a $LiNbO_3$ substrate is illustrated in Figure 7.

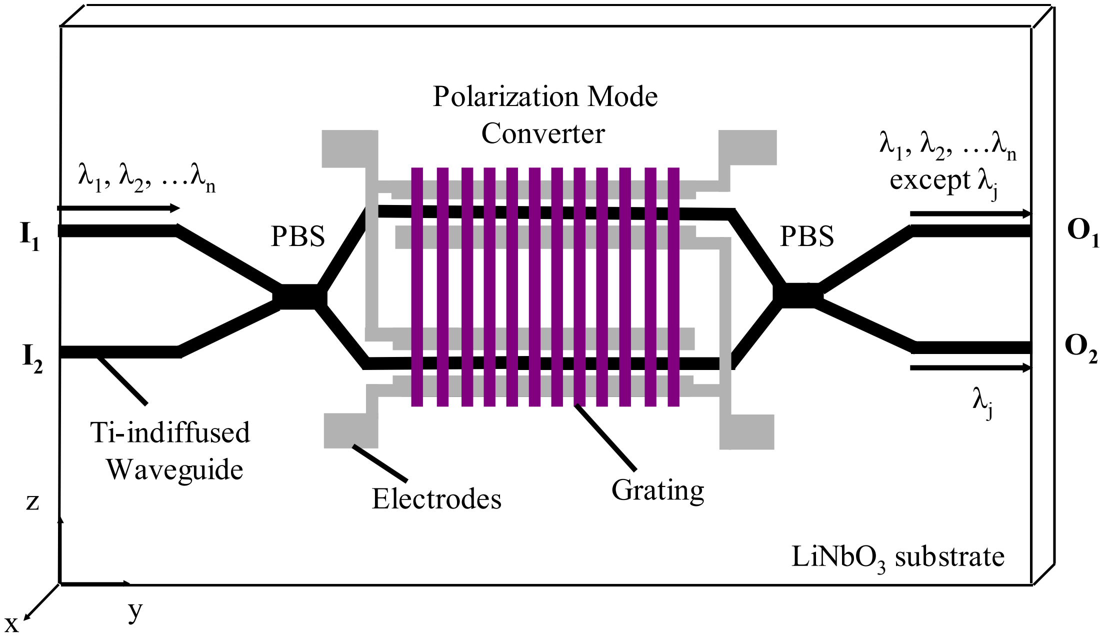

Figure 7. The structure of an integrated optical add/drop tunable filter.

The integrated tunable filter consists of two input single mode waveguides, one input polarization beam splitter (PBS), two tunable static strain-induced phase-matched polarization mode converters with one pair of electrodes, one output polarization beam splitter (PBS), and two output single mode waveguides. Incoming multiplexed signals are split into two output branches by the first polarization beam splitter based on their state of polarization (SOP). The transverse magnetic (TM) polarized modes are routed into the bar-state output while the transverse electric (TE) polarized modes are directed to the cross-state output of the splitter.

Assuming a light with wavelength components $\lambda_1, \lambda_2..., \lambda_n$ entering into the input port $I_1$, the TM- and TE-polarized modes are directed into the upper (bar-state) and lower (cross-state) arms of the first polarization beam splitter, respectively. When the separated polarized modes travel into the polarization mode converters, within each arm of the converters the polarization of one selected wavelength $\lambda_j$, which satisfies the phase-matched condition of strain-induced index gratings, is converted into its orthogonal polarization, i.e. $TM_{\lambda_j} \rightarrow TE_{\lambda_j}$ in the upper arm, and $TE_{\lambda_j} \rightarrow TM_{\lambda_j}$ in the lower arm. The second polarization beam splitter connected to the converter is identical to the first one. For those phase-mismatched signals $\lambda_1, \lambda_2..., \lambda_n$ except $\lambda_j$, ideally no polarization conversion takes place in the arms of the converter; therefore without changing the states of their polarizations as they entered into the input port $I_1$, wavelengths $\lambda_1, \lambda_2..., \lambda_n$ except $\lambda_j$ are directed towards to the output port $O_1$ (express port). The phase-matched wavelength $\lambda_j$ which experiences the mode conversion in both arms as mentioned earlier is routed towards the output port $O_2$ (drop port).

The phase-matched wavelength $\lambda_j$ can be tuned by applying a DC voltage on electrode pads since the birefringence indices change with an applied electric field via the linear electrooptic effect. Because of the symmetric device structure the phase-matched wavelength $\lambda_j$ could be added back to the rest of signals by coupling the signal $\lambda_j$ into the input port $I_2$ (add port), and the signal $\lambda_j$ emerges at the express output port $O_1$. Based on this configuration, the key components of this tunable filter are the polarization beam splitters (PBS), the polarization mode converters, and the tuning electrodes.

## B. Polarization Beam Splitters

The principle of operation of a polarization beam splitter (PBS) is based on two-mode interference in a zero-gap optical directional coupler. The basic scheme of a zero-gap directional coupler is sketched in Figure 8.

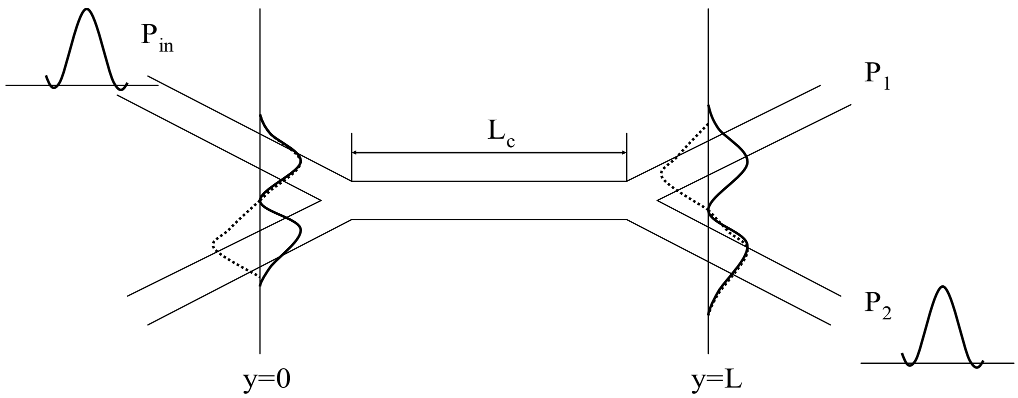

Figure 8. Basic scheme of a zero-gap directional coupler. Two lowest order local normal modes are shown.

Due to the consequence of completeness and orthogonolity, a given electric field distribution **E** corresponding to multi-modes can be expressed as [17]

$$\mathbf{E}(x,y,z)=\sum_m C_m(y)E_m(x,z)e^{-j\phi_m(y)} \tag{58}$$

where $C_m$ is the amplitude, $E_m$ is the normalized field of the local normal mode, m is a mode label and the phase function $\phi_m(y)$ is given by

$$\phi_m(y)=\beta_m y \tag{59}$$

where $\beta_m$ is the propagation constant of mode m. Assuming the mode propagation is adiabatic [17], based on two-mode interference the symmetric fundamental mode and the asymmetric lowest-order mode are excited simultaneously when the light couples into the central interaction region from one input port as shown in Figure 8 and the field distribution **E** is

$$\mathbf{E}(x,y,z)=C_sE_s(x,z)e^{-j\phi_s(y)}+C_aE_a(x,z)e^{-j\phi_a(y)} \tag{60}$$

with mode label s and a indicating the symmetric fundamental mode and the asymmetric lowest-order mode, respectively. The field contribution localized at each branch of the directional coupler can be described by the coupling between those two excited modes.

$$\begin{cases} E_1(x,z)=(1/\sqrt{2})\left[E_s(x,z)+E_a(x,z)\right] \\ E_2(x,z)=(1/\sqrt{2})\left[E_s(x,z)-E_a(x,z)\right] \end{cases} \tag{61}$$

and mode fields of $E_s$ and $E_a$ can be represented with respect to $E_1$ and $E_2$ as

$$\begin{cases} E_s(x,z)=(1/\sqrt{2})\left[E_1(x,z)+E_2(x,z)\right] \\ E_a(x,z)=(1/\sqrt{2})\left[E_1(x,z)-E_2(x,z)\right] \end{cases}. \tag{62}$$

Substituting equation (62) into (60), it yields

$$\mathbf{E}(x,y,z) = C_1(y)E_1(x,z) + C_2(y)E_2(x,z) \tag{63}$$

with

$$\begin{cases} C_1(y) = (1/\sqrt{2})\left[C_s e^{-j\phi_s(y)} + C_a e^{-j\phi_a(y)}\right] \\ C_2(y) = (1/\sqrt{2})\left[C_s e^{-j\phi_s(y)} - C_a e^{-j\phi_a(y)}\right] \end{cases}. \tag{64}$$

The power within each branch of the splitter is given by

$$P_i(y) = \left|C_i(y)\right|^2 \tag{65}$$

with i = 1,2. According to the initial conditions the input light is only launched in one branch; $P_1(0)=P_{in}$ and $P_2(0)=0$, as shown in Figure 8. Thus,

$$C_s = C_a = \sqrt{\frac{P_{in}}{2}}\,. \tag{66}$$

Substituting equations (64) and (66) into (65), it shows

$$\begin{cases} P_1(y) = P_{in}\cos^2\left(\dfrac{\Delta\phi(y)}{2}\right) \\ P_2(y) = P_{in}\sin^2\left(\dfrac{\Delta\phi(y)}{2}\right) \end{cases} \tag{67}$$

with

$$\begin{gathered} \Delta\phi(y) = \phi_s - \phi_a = \Delta\beta(y)y \\ \Delta\beta(y) = \beta_s(y) - \beta_a(y) \end{gathered}\,. \tag{68}$$

The splitting ratio is defined as

$$R = \frac{P_2}{P_1 + P_2}\,. \tag{69}$$

The output will be localized into either branch at y = L if the total phase difference $\Delta\phi(L)$ is an integer multiple of π; therefore, a light propagates towards the bar-state output for even multiples of π, and a light couples into the cross-state output for odd multiples of π. As such, a zero-gap directional coupler can act as a polarization beam splitter (PBS) if $\Delta\phi(L)$ is even multiples of π for one polarization and odd multiples of π for the other polarization. A polarization beam splitter can be decomposed into two v-junction waveguides with an opening angle α and a central two-mode interaction region of length $L_c$, as shown in Figure 9.

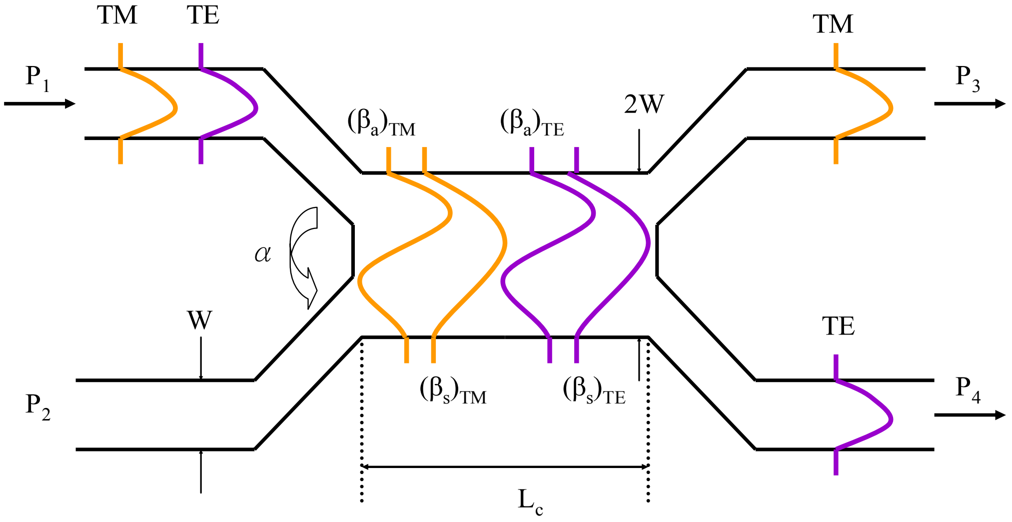

Figure 9. The structure of a polarization beam splitter based on two-mode interference.

The conditions of a polarization beam splitter are defined as [17, 18]

$$\begin{cases} \Delta\phi_{TM}(L) = \Delta\beta_{TM} L_c + 2\Delta\varphi_{TM}(\alpha) = 2m\pi \\ \Delta\phi_{TE}(L) = \Delta\beta_{TE} L_c + 2\Delta\varphi_{TE}(\alpha) = (2n-1)\pi \end{cases} \tag{70}$$

where m and n are positive integers. Here $\Delta\beta_{TM}$ is the propagation constant difference between the symmetric fundamental mode and the asymmetric lowest-order mode and $\Delta\varphi_{TM}(\alpha)$ is the generated phase difference of two excited modes in the v-junction transition region for the TM-polarized component of an input light. $\Delta\beta_{TE}$ and $\Delta\varphi_{TE}(\alpha)$ are the corresponding parameters for the TE-polarized component of an input light. The conditions expressed in equation (70) can be satisfied by a careful design of the central interaction length $L_c$ and the opening angle α, through proper fabrication parameters (i.e., initial Ti film thickness, diffusion temperature, and diffusion time). Assuming a light entering into the input port $P_1$, as shown in Figure 9, the splitting ratio in decibels, also called extinction ratio (ER), is defined as follows for TE- and TM-polarized modes and more than 20 dB is desirable.

$$\begin{aligned} (ER)_{TM} &= -10\times\log\left(\frac{P_4^{TM}}{P_3^{TM}+P_4^{TM}}\right) \\ (ER)_{TE} &= -10\times\log\left(\frac{P_3^{TE}}{P_3^{TE}+P_4^{TE}}\right) \end{aligned} . \tag{71}$$

## C. Spatially Periodic Strain-Induced Grating

The mode conversion has been discussed in the last chapter. To realize the conversion on a channel waveguide via photoelastic effect a spatially periodic strain-induced index grating is required. The periodic index grating in this study is made by a strain inducing $SiO_2$ film on the top of $LiNbO_3$ substrate. The $SiO_2$ film is deposited on the surface of $LiNbO_3$ substrate at an elevated temperature, and according to their thermal expansion coefficients the $LiNbO_3$ substrate tends to expand much more than the deposited $SiO_2$ film. The thermal expansion coefficients of $LiNbO_3$ and $SiO_2$ are $1.59 \times 10^{-5}$ [19] and $5.5 \times 10^{-7}$ [20], respectively. After cooling down to room temperature, a compressive strain is induced because the $SiO_2$ film is compressed by the $LiNbO_3$ substrate. Then a periodic grating is delineated as shown in Figure 10.

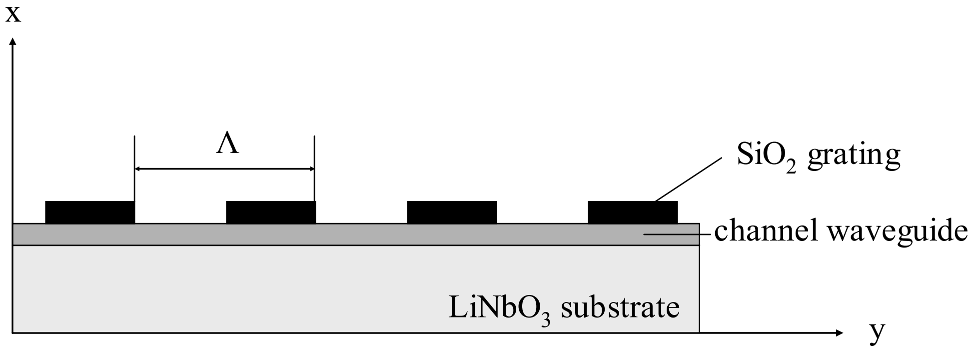

Figure 10. Longitudinal view of the periodic index grating.

The polarization coupling between TE and TM modes can be examined with this compressed strain induced between a periodic $SiO_2$ film and the $LiNbO_3$ substrate. Only the displacement along the y-direction from (x, y, z) to (x, y+$u_y$, z) is relevant. The displacement $u_y$ varies continuously with the position x. Therefore, only the shear-strain component $S_6$ exists and contributes to polarization conversion, and $S_6$ is given by [21]

$$S_6 = \frac{1}{2}\frac{\partial u_y}{\partial x}. \tag{72}$$

The photoelastic tensor $P_{\alpha\beta}$ of a $LiNbO_3$ substrate is [14]

$$P_{\alpha\beta} = \begin{pmatrix} P_{11} & P_{12} & P_{13} & P_{14} & 0 & 0 \\ P_{12} & P_{11} & P_{13} & -P_{14} & 0 & 0 \\ P_{13} & P_{13} & P_{33} & 0 & 0 & 0 \\ P_{41} & -P_{41} & 0 & P_{44} & 0 & 0 \\ 0 & 0 & 0 & 0 & P_{44} & P_{41} \\ 0 & 0 & 0 & 0 & P_{14} & \tfrac{1}{2}(P_{11}-P_{12}) \end{pmatrix}. \tag{73}$$

Based on the earlier analysis results shown in equations (51) and (52), the induced refractive index change $\Delta n_5$ caused by the photoelastic effect leads to the polarization conversion. By substituting equation (73) into (39) with only shear strain component $S_6$, $\Delta n_5$ is obtained as

$$\Delta n_5 = -\frac{1}{2}\bar{n}^3 P_{41} S_6 \tag{74}$$

with $\bar{n} = \sqrt{n_o n_e}$ , where $n_o$ and $n_e$ are ordinary and extraordinary refractive indices, respectively. The strain component $S_6$ can be calculated based on relaxation theory [22], and from an earlier report [23] the maximum calculated $|S_6|$ is $2.6 \times 10^{-4}$ under the condition that a 1.45 μm thick $SiO_2$ film is deposited at 360°C and the periodic pattern with $\Lambda$ = 21 μm is delineated at the room temperature. The induced index change $\Delta n_5$ on a $LiNbO_3$ substrate with a strain-induced grating can be obtained with the photoelastic coefficient $P_{41} = -0.15$ [24] and $\bar{n} \sim 2.17$. ($n_o \sim 2.21$ and $n_e \sim 2.14$ at 24.5°C for 1550 nm wavelength [25]) The calculated index change $\Delta n_5$ is $\sim 2.0 \times 10^{-4}$.

### D. TE↔TM Polarization Mode Converters

A polarization mode converter can be produced in a single-mode Ti-indiffused channel waveguide with a spatially periodic strain-induced index grating on a $LiNbO_3$ substrate, as illustrated in Figure 11.

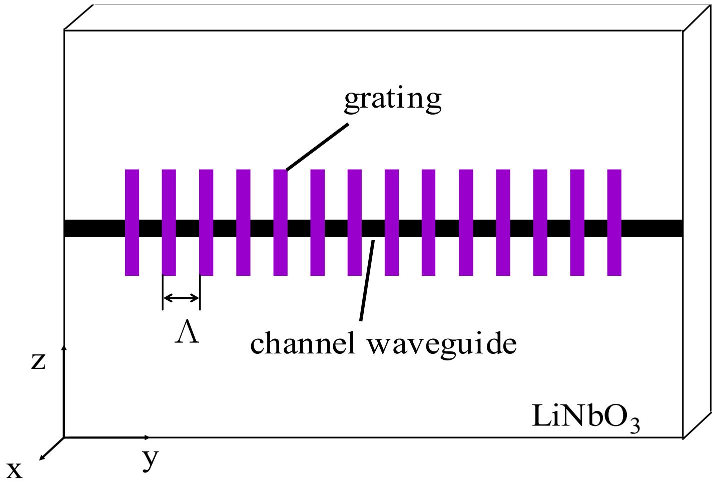

Figure 11. The basic structure of a polarization mode converter.

Assuming a TM-polarized light is coupled into the channel waveguide, due to coupled-mode theory [12] as discussed in the previous chapter with initial conditions $A_{TM}(0) = a_o$ and $A_{TE}(0) = 0$, the normalized transmitted TE-polarized power of the converter is given by

$$I_{out}(L) = \frac{|A_{TE}(L)|^2}{|a_o|^2} = \frac{\kappa^2}{(\kappa^2+\delta^2)} \sin^2\left[\sqrt{(\kappa^2+\delta^2)}\, L\right] \tag{75}$$

where L = NΛ with N the total number of periodic uniform gratings; κ is the coupling coefficient and κL = π/2 for the complete TM→TE mode conversion. In the conversion process, the wavelength deviation Δλ from the phase-matched wavelength $\lambda_o$ introduces a phase-mismatch factor δ which can be expressed as [26]

$$\delta(\Delta\lambda) \cong \Delta\lambda\left[\frac{d}{d\lambda}\left(\frac{\beta_{TM}(\lambda)-\beta_{TE}(\lambda)}{2}\right)\right]\Bigg|_{\lambda=\lambda_o} = -\frac{\Delta\lambda}{\lambda_o}\frac{\pi}{\Lambda}\frac{\Delta n_g(\lambda_o)}{\Delta n_p(\lambda_o)} \tag{76}$$

with

$$\begin{aligned} \Delta n_p(\lambda_o) &= n_{TM}(\lambda_o) - n_{TE}(\lambda_o) \\ \Delta n_g(\lambda_o) &= \Delta n_p(\lambda_o) - \lambda_o\left(\frac{d\Delta n_p(\lambda_o)}{d\lambda}\right)\Bigg|_{\lambda=\lambda_o} \end{aligned} \tag{77}$$

where $\Delta n_p(\lambda_o)$ and $\Delta n_g(\lambda_o)$ denote the phase and group effective index difference, respectively between TE and TM modes at design wavelength $\lambda_o$. Neglecting the first order of $\Delta n_g(\lambda_o)$ for simplicity, the factor δ becomes

$$\delta(\Delta\lambda) = -\frac{\Delta\lambda}{\lambda_o}\frac{\pi}{\Lambda}. \tag{78}$$

Substituting equation (78) into (75) and κL = π/2 for the complete conversion, the converted output power $I_{out}$ dependence on the wavelength deviation Δλ is obtained as

$$I_{out}(\Delta\lambda) = \frac{\pi^2}{\pi^2 + \left[2\delta(\Delta\lambda)L\right]^2}\sin^2\left(\frac{1}{2}\sqrt{\pi^2 + \left[2\delta(\Delta\lambda)L\right]^2}\right). \tag{79}$$

The output transmission is highly wavelength-dependent, as shown in Figure 12. The -3 dB bandwidth (FWHM) of a polarization mode converter can be obtained by substituting equation (78) into (79) as [27]

$$(\Delta\lambda)_{FWHM} \sim 0.8\frac{\Lambda}{L}\lambda_o = 0.8\frac{\lambda_o}{N}. \tag{80}$$

An important parameter for the characterization of a TE↔TM polarization mode converter is the conversion efficiency defined as

$$\eta_{TE} = \frac{(P_{out})_{TM}}{(P_{out})_{TE} + (P_{out})_{TM}} \tag{81}$$

with TE-polarized input, and

$$\eta_{TM} = \frac{(P_{out})_{TE}}{(P_{out})_{TE} + (P_{out})_{TM}} \tag{82}$$

with TM-polarized input where $(P_{out})_{TE}$ and $(P_{out})_{TM}$ are TE- and TM-polarized output powers, respectively. The conversion efficiency is ideally equal to one if the complete conversion occurs at the phase-matched wavelength.

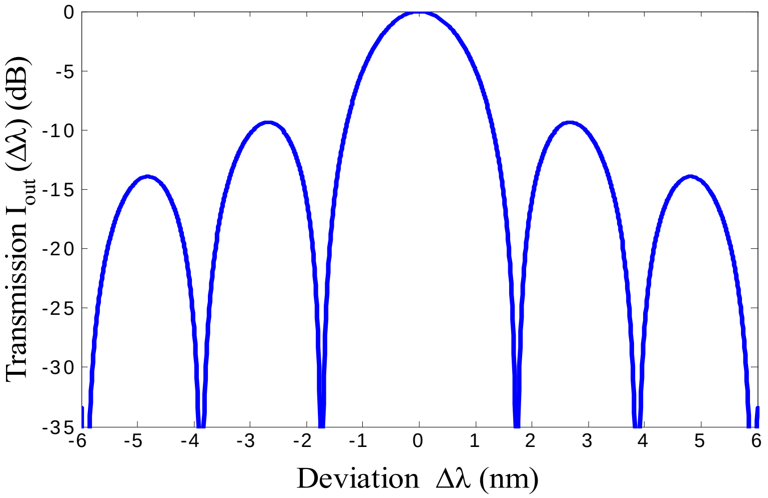

Figure 12. Normalized converted power transmission with wavelength deviation from center wavelength 1530 nm for N = 765 periodic uniform gratings.

## E. Electrooptic Tuning

To make a tunable polarization mode converter a pair of electrodes is placed on either side of a channel waveguide. According to the linear electrooptic effect, refractive indices can be changed via an applied DC voltage to the electrodes along the optic axis (z-direction). Since neither the applied electric field nor the optical mode field is uniform, an overlap factor Γ is introduced, which is defined as the overlap integral between the applied electric field and the optical field [28]. Equation (28) becomes

$$\begin{aligned} n_{TM} &= n_x = n_o - \frac{1}{2}\Gamma_{TM} n_o^3 r_{13} \frac{V_T}{g} \\ n_{TE} &= n_z = n_e - \frac{1}{2}\Gamma_{TE} n_e^3 r_{33} \frac{V_T}{g} \end{aligned} \tag{83}$$

where $\frac{V_T}{g} = E_Z$ and g is the gap between electrodes; $\Gamma_{TM}$ and $\Gamma_{TE}$ are overlap factors for TM- and TE-polarized modes, respectively. The refractive index difference Δn between two polarizations yields

$$\Delta n = \left| n_{TM} - n_{TE} \right| = \left| \left( n_o - n_e \right) - \frac{1}{2}\left( \Gamma_{TM} n_o^3 r_{13} - \Gamma_{TE} n_e^3 r_{33} \right) \frac{V_T}{g} \right| \tag{84}$$

Substituting equation (84) into (57), and taking the derivative of $\lambda_o$ with the applied DC tuning voltage $V_T$, the electrooptic tuning rate is expressed by

$$\frac{d\lambda_o}{dV_T} = \frac{1}{2}\left( \Gamma_{TM} n_o^3 r_{13} - \Gamma_{TE} n_e^3 r_{33} \right) \frac{\Lambda}{g}. \tag{85}$$

From the above analysis, a tunable TE↔TM polarization mode converter is regarded as the key mechanism for a tunable add/drop filter.

# CHAPTER IV

# DEVICE FABRICATION

The fabrication process of the integrated tunable add/drop filter is presented in this chapter. The tunable filter consists of two main components: a polarization beam splitter (PBS) and a tunable TE↔TM polarization mode converter. The fabrication procedure and physical configuration of those two devices will be described in following sections.

## A. Ti-Indiffused Channel Waveguides and Polarization Beam Splitters

There are different ways to make optical waveguides on a $LiNbO_3$ substrate. Ti-indiffused waveguides are adapted here for simplicity and low insertion loss. Individual components can be integrated easily on one chip with thermal indiffusion of a Ti film.

The fabrication of straight channel waveguides and polarization beam splitters began with dicing a 1 mm thick, 3 inch diameter, x-cut $LiNbO_3$ crystal wafer supplied by Crystal Technology Inc. (Palo Alto, CA) into appropriate sizes (Appendix 1) for making devices with the lightwave propagation along y-direction. The wafer was diced into 9 mm (z-direction) by 14 mm (y-direction) for channel waveguides and 9 mm by 25 mm for polarization beam splitters. The diced samples were cleaned with liquid solvents (Appendix 2) and a Ti film (~ 1050 Å Ti thickness for channel waveguides and ~1330 Å Ti thickness for splitters) was deposited over the substrate surface using a DC Sputtering process (Appendix 3). After Ti-film deposition, the patterns of channel waveguides and splitters were delineated with AZ-5214 photoresist made by Clariant via positive photolithography (Appendix 4). The photoresist-coated sample was physically contacted with a mask, known as contact printing, and the photoresist was exposed to a nearly collimated ultraviolet (UV) beam for a fixed time. The photoresist-coated patterns were formed after developing in a diluted Shipley MF312 developer. The samples were inspected with a microscope for the quality of photoresist-coated patterns.

To ensure that there was no residue of exposed photoresist left after developing, the samples were further cleaned in a barrel asher with $O_2$ plasma (Appendix 6) for 2 minutes, and hard baked under vacuum at 135°C for 5 minutes to harden the photoresist so that it could sustain later etching processes. The non-patterned Ti film was mainly etched away using reactive ion etching (RIE) (Appendix 7). Since the gases ($CHF_3$: 75 sccm, Argon: 2 sccm, and Helium: 7.5 sccm) used in RIE could also slightly etch through the $LiNbO_3$ substrate if over-etched, it was important to etch the Ti film carefully until only a very thin Ti layer was left to protect the substrate. For Ti film thickness of 1350 Å it took ~ 12 minutes under RIE at 350 watts plasma power. The residual Ti film was etched away using diluted hydrofluoric acid (HF). Since the wet-etching process is isotropic, the appropriate acid solution and etching time were required to produce straight patterns. A light could not be confined in a channel waveguide and causes planar surface-guiding if under-etched, while a guided light would scatter away from a rough surface edges if over-etched. The acid solution used here was $HF:H_2O$ = 1:25 etched for 10 ~ 12 seconds to produce satisfactory patterns. The photoresist was then completely removed by leaving samples in a heated 90°C photoresist stripper

(Clariant AZ 300T) for 15 minutes and the samples were cleaned with liquid solvents (Appendix 2).

The patterns for channel waveguides were designed with various waveguide widths ranging from 5 µm to 10 µm and the delineated patterns for polarization beam splitters consisted of two v-junction waveguides with a splitting angle α and a central interaction region of width h and length $L_c$ (ranging from 200 µm to 280 µm), as shown in Figure 13. Further details are given in Appendix 8. The width of Ti strip was inspected with a high magnification microscope and the thickness of Ti film was measured using Dektak$^3$ Surface Profile Measuring System (Appendix 9).

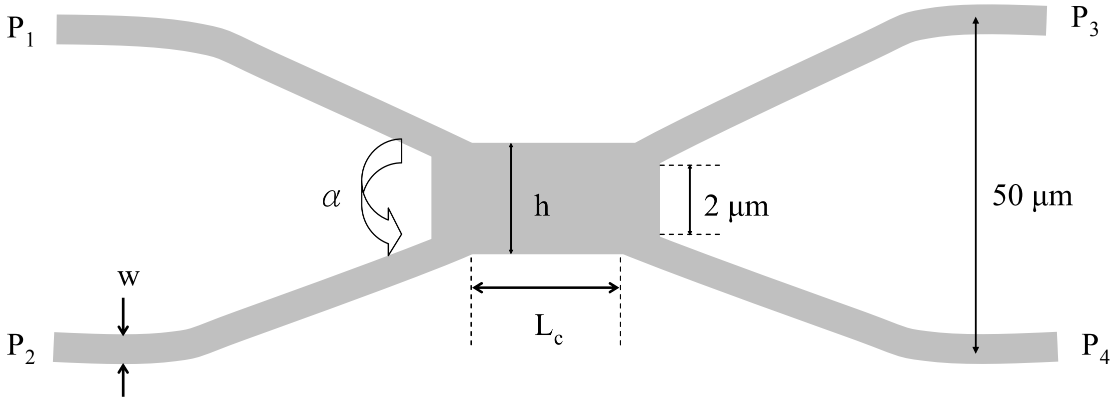

Figure 13. The structure of a polarization beam splitter with a splitting angle α and a central interaction length $L_c$.

The samples were then put inside a furnace for diffusion under wet air ambient at certain fixed temperatures ranging between 1025°C to 1055°C for 9 to 11 hours depending on the deposited Ti film thickness (Appendix 10). The initial Ti thickness τ, diffusion temperature T, and diffusion time t are three key parameters for making good quality waveguides with single mode propagation, low propagation loss, well confined mode profiles for both TE and TM polarizations, and high extinction (splitting) ratios for polarization beam splitters. The diffusion depth d is described by the diffusion temperature T and time t as [29]

$$d = 2\sqrt{Dt} \tag{86}$$

with the diffusion coefficient D given by

$$D = D_o e^{-\frac{T_o}{T}} \tag{87}$$

where $D_o$ is the bulk diffusivity and $T_o$ is the activation temperature depending on the composition of a $LiNbO_3$ crystal [30]. Profiles of electric field distributions on a diffused channel waveguide are illustrated in Figure 14 [31] where $\sigma_1$ and $\sigma_2$ are 1/e of the maximum intensity of the asymmetric depth profile $E_x$ employing two half–Gaussian; $\sigma_3$ is half width of 1/e of the maximum intensity of the symmetric Gaussian lateral profile $E_y$.

During diffusion care must be taken to avoid surface guiding that could occur for the z-direction polarized mode i.e., the TE-polarized mode with the extraordinary refractive index. Surface guiding is induced by $Li_2O$ out-diffusion in dry ambient and leads to significant propagation loss. To eliminate out-diffusion the option adapted here was bubbling air through a room temperature water column before it flows into the furnace to create the wet atmosphere [32]. At last both ends of the samples were polished (Appendix 11) to produce smooth xz-transverse end faces perpendicular to the light propagating direction (y-axis) for optical testing.

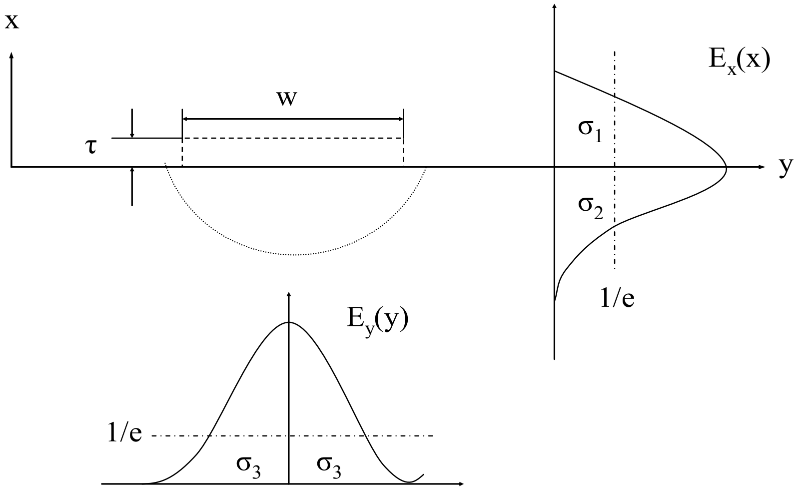

Figure 14. The schematic profile of field distributions for a diffused channel waveguide.

## B. Tunable TE↔TM Polarization Mode Converters

A tunable polarization mode converter consists of three parts: a single-mode Ti-indiffused channel waveguide, one pair of electrodes for electrooptic tuning, and a spatially periodic strain-induced index grating for TE↔TM polarization conversion on a $LiNbO_3$ substrate. The structure of a tunable TE↔TM polarization mode converter is sketched in Figure 15.

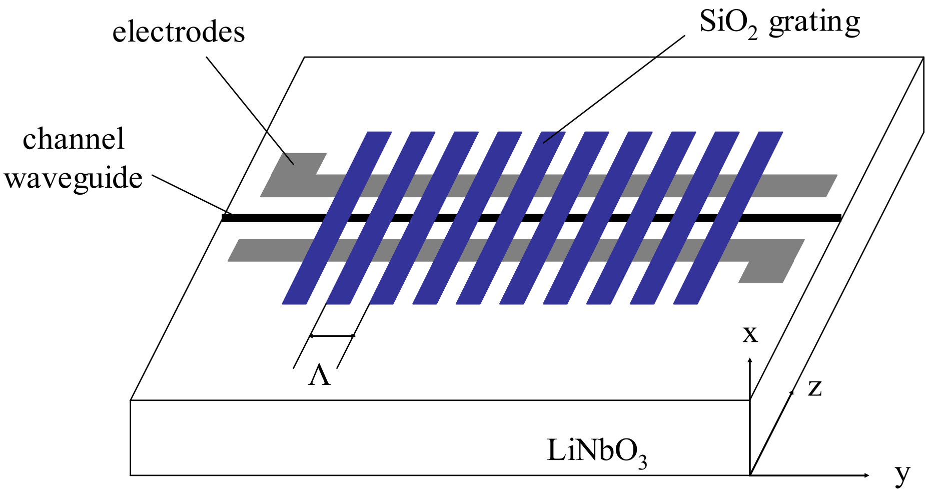

Figure 15. The diagram of a tunable TE↔TM polarization mode converter.

First the straight channel waveguides of 7 μm width were obtained as described in section A and tested to ensure single-mode propagation, low insertion loss, and good confinement for both polarization modes. Next one pair of electrodes was placed on either side of the channel waveguide. To make the electrodes, patterns were delineated first using image reversal photolithography process (Appendix 12). The dimension details are given in Appendix 15. The samples were then further cleaned using a barrel asher under $O_2$ descum for 2 minutes. Once the patterns were made, three different metal layers were deposited in order of Cr/Au/Ti with the thickness of 650Å/800Å/650Å, respectively using e-beam evaporation (Appendix 13). The Cr layer was used to improve the adhesion between the metal layers and the $LiNbO_3$ substrate, and the Ti layer was used to prevent Au from diffusing into $SiO_2$ film of later deposition processes. The Cr/Au/Ti electrodes were produced by a lift-off process in acetone.

The final step is to create a spatially periodic strain-induced index grating. The $LiNbO_3$ substrate with Ti-indiffused waveguides and electrodes was heated up slowly until stabilized at 360°C, and a thick layer of $SiO_2$ film of 1.45 μm was deposited by e-beam evaporation at this elevated temperature with $O_2$ flowing inside the chamber. After completing the $SiO_2$ deposition, the sample was kept inside the chamber with $O_2$ continuously flowing until cooling down to the room temperature. The $O_2$ flowing during the $SiO_2$ deposition and the cooling time was to avoid $O_2$ out-diffusion from the $LiNbO_3$ substrate. A uniform periodic grating of the $SiO_2$ film was delineated using positive photolithography with longer dehydration time and higher soft-bake temperature (Appendix 5) than the channel waveguides patterned process. The sample was then vacuum hard-baked at 135°C for 11 minutes and dry etched under RIE system for 20 minutes with 300 watts plasma power. The non-patterned $SiO_2$-film residue after RIE was completely removed by wet-etching in buffered oxide etch (BOE) for 25~30 seconds. The photoresist on top of $SiO_2$ grating patterns was cleaned by leaving the sample in heated 90°C photoresist stripper for 10 minutes. A total number of 765 uniform index gratings with a spatial period $\Lambda$ of 21 μm was obtained. Then the sample was ready for optical testing.

### C. Electrooptically Tunable Add/Drop Filters

The electrooptically tunable add/drop filter was made on an x-cut y-propagating $LiNbO_3$ substrate with the size of 16.5 mm (z-axis) by 62 mm (y-axis). The principle of operation has been discussed earlier and the schematic of a complete filter structure is illustrated in figure 16. The details of the filter design are given in Appendix 14.

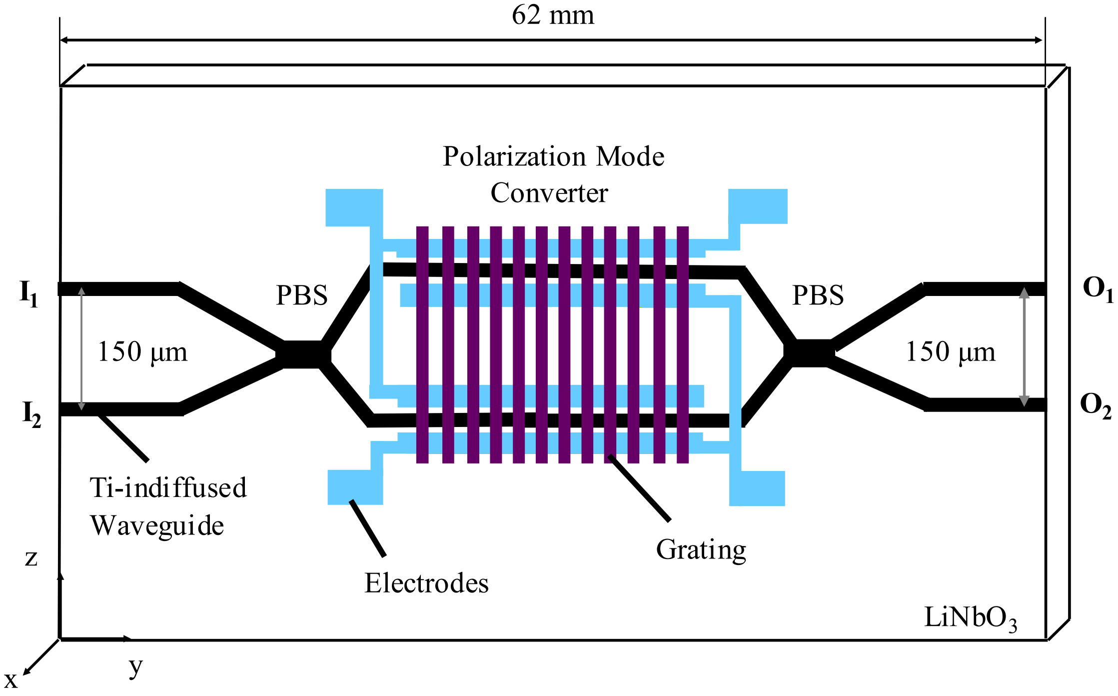

Figure 16. The schematic of the complete tunable add/drop integrated filter structure.

The complete filter consisting of three layers in a sequence of Ti-indiffused waveguides, electrooptic tuning electrodes, and $SiO_2$ gratings was fabricated using similar procedures as making the tunable polarization mode converter. First, the Ti-indiffused waveguides including input and output single-mode waveguides, two polarization beam splitters and channel waveguides of the tunable polarization mode converters were integrated on a $LiNbO_3$ substrate made with 1350 Å deposited Ti film thickness and diffused at 1055°C for 9 hours. Once the first layer was produced, the overall splitting ratio was measured using fiber coupling before proceeding to the next fabrication step. Second, Cr/Au/Ti metal layers of the corresponding thickness 650Å/800Å/650Å were deposited on the substrate of delineated photoresist electrode patterns, and the electrode pairs were formed after lift-off process in acetone. Third, the 765 uniform periodic strain-induced index gratings made from a 1.41 µm thick $SiO_2$ film was fabricated on top of the electrode pairs using e-beam evaporation system to deposit a $SiO_2$ film at 360°C, and positive photolithography to produce the grating patterns. Finally, the characterizations of the complete tunable add/drop optical filter were performed under fiber coupling.

# CHAPTER V

# OPTICAL TESTING AND RESULT ANALYSIS

In this chapter the optical testing performance of channel waveguides, polarization beam splitters, and tunable TE↔TM Polarization mode converters are presented. The characteristics of an optical tunable add/drop filter with respect to overall extinction ratio, field distribution profiles, electrooptic tuning, temperature and polarization dependence are analyzed.

## A. Channel Waveguides

To achieve good performance from an integrated optical filter, high quality channel waveguides are required. A high quality channel waveguide should have single mode propagation, low insertion loss, and strong confinement of near field distributions for both TE and TM polarizations. Those qualities can be optimized by controlling fabrication parameters which consist of initial thickness of Ti strip, the width of a channel waveguide, diffusion temperature, and diffusion time. The insertion loss of a waveguide is the total amount of lost intensity after placing a waveguide in-between an optical path, and it is defined in dB as

$$Insertion\,Loss(dB) = -10\log\left(\frac{P_{out}}{P_{in}}\right) \tag{88}$$

where $P_{in}$ and $P_{out}$ are input and output powers to the waveguide, respectively. The test arrangement for the insertion loss measurement is shown in Figure 17. A pigtailed 1.55

μm distributed feedback (DFB) laser diode (AT&T, Model 225) driven by a current source (ILX Lightwave, Model LDX-3412) at 32 mA was used as an optical source. The pigtail fiber was spliced to a single mode fiber (Corning SMF-28$^{TM}$) and the fiber was routed into a fiber polarization controller (Thorlabs Inc., Model FDC010) to switch the polarization state of an input light. The sample was placed on a high resolution x-y-z translation stage (Line Tool Co., Allentown, PA), and the light was butt coupled into the waveguide via a flat-polished edge. A 20× objective lens was placed at the output to collect the light and focus it onto a Ge photodetector (Newport, Model 818-IR) and the output power was measured with a power meter (Newport, Model 1825-c).

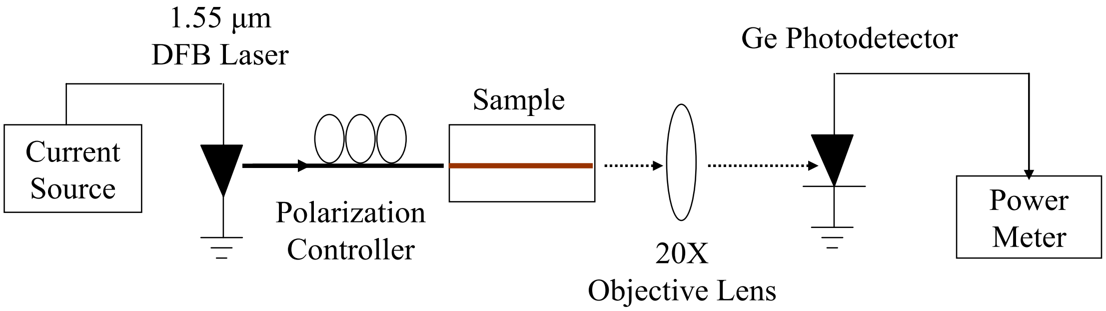

Figure 17. The test arrangement of the insertion loss measurement.

Several samples with different Ti film thicknesses, waveguide widths, and diffusion conditions were fabricated. The sample k106 with Ti film thickness of 1089 Å diffused at 1025°C for 11 hours was tested. The size of sample k106 is 14 mm long and the waveguide widths ranged from 5 μm to 10 μm. Table 2 shows the insertion loss with respect to various waveguide widths.

Table 2. Insertion loss of channel waveguides for TE and TM polarizations with various widths on sample k106 diffused at 1025°C for 11 hours.

| Waveguide width (μm) | 5 | 6 | 7 | 8 | 9 | 10 |
|---|---|---|---|---|---|---|
| TM mode loss (dB) | 30 | 10.36 | 3.81 | 3.05 | 3.02 | 3.0 |
| TE mode loss (dB) | 6.02 | 3.65 | 3.43 | 3.13 | 3.46 | 3.60 |

Waveguide widths of 7 μm and 8 μm with Ti film thickness of 1000 ~ 1300 Å are commonly used for maintaining single mode propagation. The wider width may excite asymmetric mode simultaneously and cause multi-mode propagation. The dependence of the insertion loss for 7 μm and 8 μm waveguide widths on diffusion time is given in Table 3, and it shows the insertion loss decreases with longer diffusion time due to greater refractive index change.

Table 3. Insertion loss of 7 μm and 8 μm wide waveguide widths on sample k106 with different diffusion time for TE and TM polarizations.

| Diffusion time (hours) | | 9 | 9+1 | 9+1+1 |
|---|---|---|---|---|
| 7 μm | TM mode loss (dB) | 6.52 | 4.54 | 3.81 |
| | TE mode loss (dB) | 4.85 | 3.92 | 3.43 |
| 8 μm | TM mode loss (dB) | 3.42 | 3.16 | 3.05 |
| | TE mode loss (dB) | 4.81 | 3.46 | 3.13 |

There are three primary loss components contributing to the fiber-waveguide insertion loss: 1) Fresnel loss, 2) mode mismatch loss, and 3) propagation loss [33]. The Fresnel loss results from the reflections of an optical field at both ends of a waveguide and can be estimated by assuming the effective indices seen by TE and TM modes in a waveguide are equal to the extraordinary index $n_e$ and the ordinary index $n_o$, respectively. An estimation of Fresnel loss is given by

$$Fresnel\,loss(dB) = Loss_f = -2\times 10\log(1-R) \tag{89}$$

with

$$R = \left(\frac{1-n_i}{1+n_i}\right)^2 \tag{90}$$

where $n_i$ = $n_o$ or $n_e$ depending on the polarization state of the propagating mode. The Fresnel loss can be reduced with an index-matched fluid or an antireflection coating at the edges of a waveguide [34]. The mode mismatch loss is caused by the different field profiles between an optical fiber and the propagation mode of a waveguide, and it can be determined by evaluating the overlap integral between the electric field profile of an optical fiber and the channel waveguide. Assuming circular Gaussian profile of the fiber mode and employing two half-Gaussian profiles of a waveguide as depicted in Figure 14, the mode mismatch is expressed as [31, 33]

$$mode\,mismatch\,loss\,(dB) = Loss_m = -10\log\eta \tag{91}$$

with the coupling efficiency $\eta$, given as

$$\eta = \frac{2\left(\left(\frac{1}{a^2}+\frac{1}{\sigma_1^2}\right)^{-\frac{1}{2}}+\left(\frac{1}{a^2}+\frac{1}{\sigma_2^2}\right)^{-\frac{1}{2}}\right)^2}{a^2\sigma_3\left(\sigma_1+\sigma_2\right)\left(\frac{1}{a^2}+\frac{1}{\sigma_3^2}\right)} \tag{92}$$

where $a$ is the mode diameter of fiber; $\sigma_1$ and $\sigma_2$ are 1/e of maximum intensity of the asymmetric depth profile and $\sigma_3$ is half width of 1/e of maximum intensity of the symmetric lateral profile of the waveguide. Once the insertion loss, Fresnel loss, and mode mismatch loss are known, the propagation loss for the waveguide can be obtained in the unit of dB/cm as

$$Propagation\,loss\left({}^{dB}\!/_{cm}\right) = \frac{insertion\,loss-\left(Loss_f + Loss_m\right)}{L} \tag{93}$$

where L is the propagation length.

Another feature to inspect in a channel waveguide is the near field intensity profile. A setup for the mode profile measurement is illustrated in Figure 18.

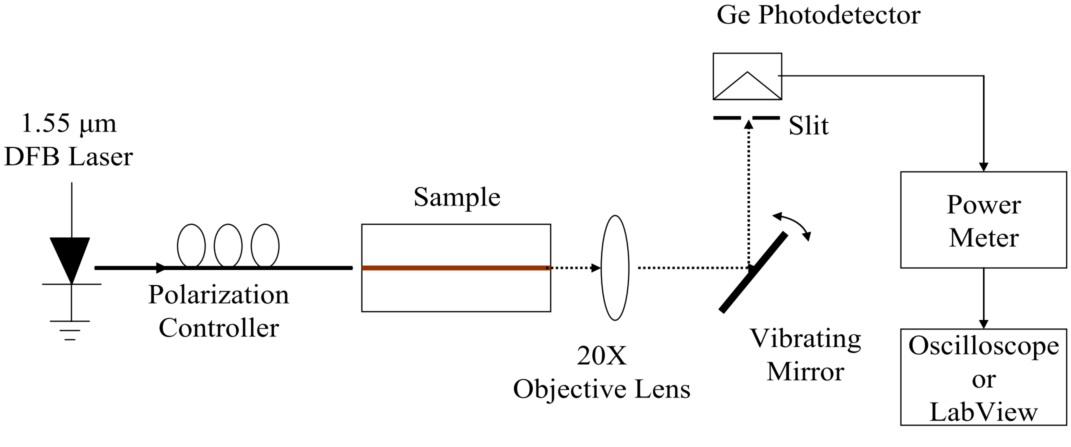

Figure 18. The test setup of the mode profile measurement.

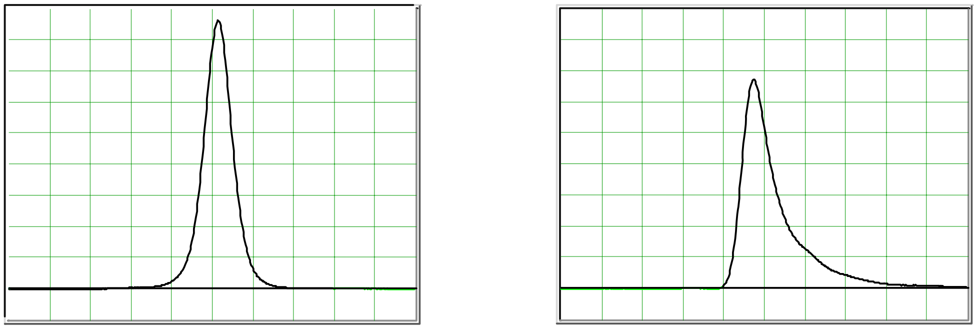

(a) Horizontal scan of TM mode (b) Vertical scan of TM mode

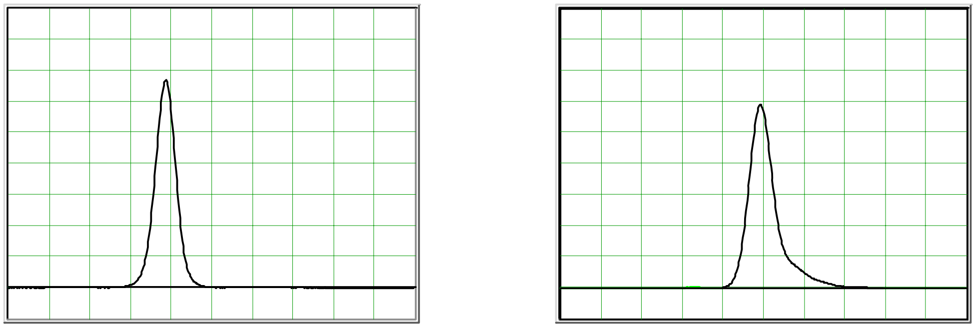

(c) Horizontal scan of TE mode (d) Vertical scan of TE mode

Figure 19. Mode Profiles of the 7 μm wide channel waveguide on sample k106. Horizontal scale is 10.37 μm/div and vertical scale is 100 mV/div.

The arrangement is the same as the one used for the insertion loss measurement, but before the light is launched onto the photodetector, a vibrating mirror and a 100 μm wide slit are placed in the optical path to deflect light for the profile test. The vibrating mirror was driven by a circuit for a beam scanning horizontally or vertically across the waveguide edge. The slit was inserted in front of the photodetector for improving the spatial resolution, and it was oriented vertically for horizontal scans and horizontally for vertical scans to obtain transverse lateral and transverse depth near field intensity profiles, respectively. The optical power meter was connected to an oscilloscope for direct display, or a computer via a NI-DAQ board (National Instruments – Data Acquisition) for storage. The storage data can be acquired with the LabVIEW program.

Figure 19 shows the measured mode profiles of transverse lateral and depth distributions for both TE and TM polarizations on a 7 μm wide waveguide of sample k106. The mode profile display clearly exhibits the waveguide supporting only single mode propagation for both TE and TM polarizations since there is only one peak showing in the profile display. The transverse lateral profile of horizontal scans reveals a symmetric Gaussian shape while the transverse depth profile of vertical scans shows an asymmetric shape corresponding to the field distributions depicted in Figure 14. Full Width at Half Maximum (FWHM) was used to evaluate the mode confinement. To measure FWHM a directional coupler with two output branches separated at 68 μm was used as a scale. The measured FWHM of 7 μm and 8 μm wide channel waveguides of sample k106 for both TE and TM polarizations are given in Table 4. It shows the TE-polarized mode has stronger confinement than the TM-polarized mode.

Table 4. Measured FWHM of 7 μm and 8 μm wide channel waveguides on sample k106 with 1089 Å Ti thickness and diffused at 1025 ºC for 9 hours.

| Waveguide width | 7 μm | | 8 μm | |
|---|---|---|---|---|
| | TM mode | TE mode | TM mode | TE mode |
| FWHM (μm) of horizontal scan | 8.30 | 6.06 | 7.85 | 5.83 |
| FWHM (μm) of vertical scan | 8.30 | 7.18 | 8.75 | 6.73 |

## B. Polarization Beam Splitters

For an optical element, the state of polarization is an important factor. To have a compact and versatile optical tunable filter device, polarization independence is needed and a polarization beam splitter as shown in Figure 20 is introduced for this purpose based on two-mode interference phenomenon in the central interaction region. The splitter can be integrated with other elements on the same chip to form a polarization independent optical filter.

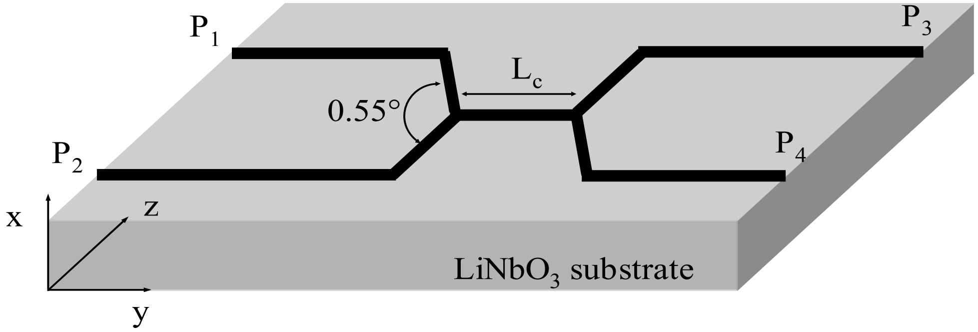

Figure 20. The schematic diagram of a polarization beam splitter.

The performance of a polarization beam splitter can be evaluated from its extinction ratio (ER), as defined in equation (71). Assuming a TE- or TM-polarized light is coupled into port $P_1$, the intensity profiles of output ports $P_3$ and $P_4$ are scanned with a vibrating mirror using the same setup as Figure 18. Figure 21 shows the measured mode profile of a polarization beam splitter on sample ks28 indicating extinction ratio of 9.06 dB for the TE polarization. The tested splitter on sample ks28 was made using 1327 Å Ti film thickness with 1055°C diffusion temperature for 9 hours, and had a 7 μm wide waveguide width with a 240 μm long central interaction length.

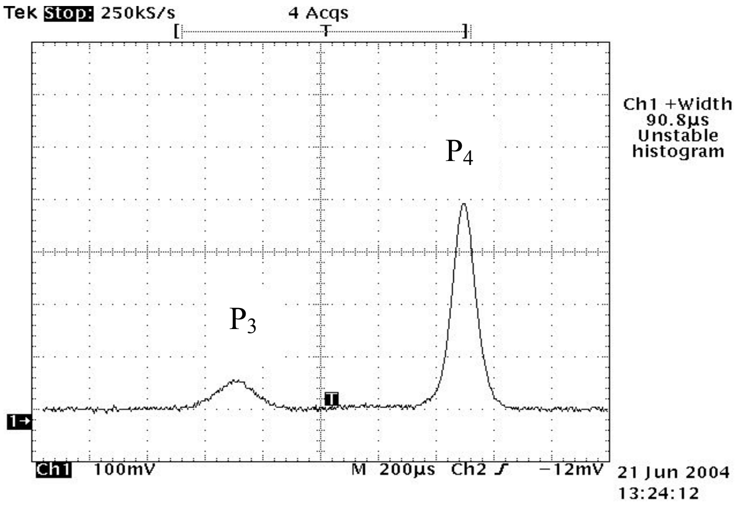

Figure 21. Measured mode profile of the polarization beam splitter tested with 240 μm long interaction length of sample ks28 with extinction ratio 9.06 dB for the TE polarization. Horizontal scale is 10.37 μm/div and vertical scale is 100 mV/div.

The extinction ratio was obtained by measuring the power from two output ports of a splitter using the arrangement depicted in Figure 22. Amplified Spontaneous Emission (ASE) light from an Erbium-Doped Fiber Amplifier (EDFA) was used as a broadband input source. The reason for using a broadband light source was to ensure proper operation when integrated with polarization mode converters in the formation of a tunable filter. The ASE light was connected to a polarizing single mode fiber (PZ fiber) that can be rotated to select either TE- or TM-polarized input. The output light was coupled into a single mode fiber and detected by a Ge photodetector connected to a power meter.

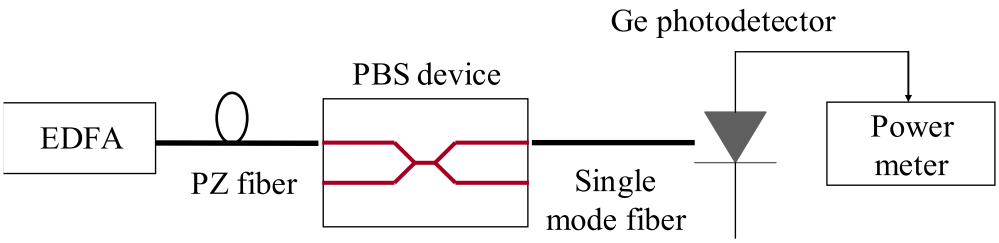

Figure 22. The test arrangement for measuring extinction ratio.

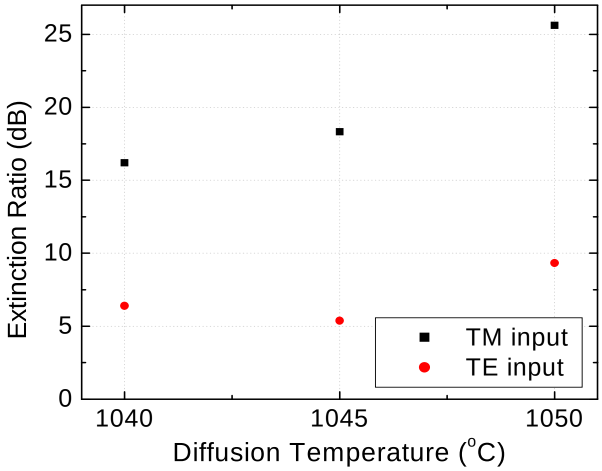

Figure 23. The measured ER of samples ks15, ks9, and ks8 with Ti film thicknesses corresponding to 1199 Å, 1227 Å, and 1228 Å diffused at three different temperatures of 1040°C, 1045°C, and 1050°C, respectively for 9 hours for both TE and TM modes.

Numerous samples with polarization beam splitters that were produced under various fabrication parameters have been tested. The mask design of polarization beam splitters is given in Appendix 8. The extinction ratio (ER) is determined with three critical fabrication parameters: 1) initial Ti film thickness, 2) diffusion temperature, and 3) diffusion time. In what follows, test results regarding those parameters are presented. The ER of three samples ks15, ks9, and ks8 with close Ti film thicknesses corresponding to 1199 Å, 1227 Å, and 1228 Å, diffused at three different temperatures of 1040°C, 1045°C, and 1050°C, respectively for 9 hours is shown in Figure 23 for both TE and TM modes. Figure 24 shows the ER of various deposited Ti film thicknesses, all diffused at 1050°C for 9 hours, for both TE and TM modes.

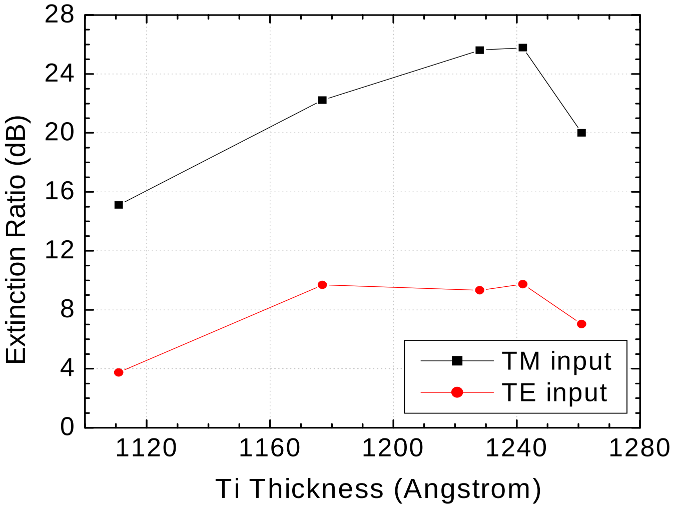

Figure 24. The ER of samples ks22, ks4, ks8, ks7, and ks12 with corresponding Ti film thicknesses of 1111Å, 1177Å, 1228Å, 1242Å, and 1261Å all diffused at 1050°C for 9 hours for TM and TE modes.

Since the TM polarization produced much better extinction ratios than the TE polarization for all the different diffusion temperatures and Ti film thicknesses, as shown in Figure 23 and 24, the use of thicker Ti film was explored to improve the extinction ratio of the TE polarization. Figure 25 shows the optimized results of the TE mode with much thicker Ti film thicknesses diffused at a higher temperature of 1055°C, and all for 9 hours. The ER values shown in Figure 23, 24, and 25 were all measured on splitters having a 280 μm long central interaction length due to their better splitting performance.

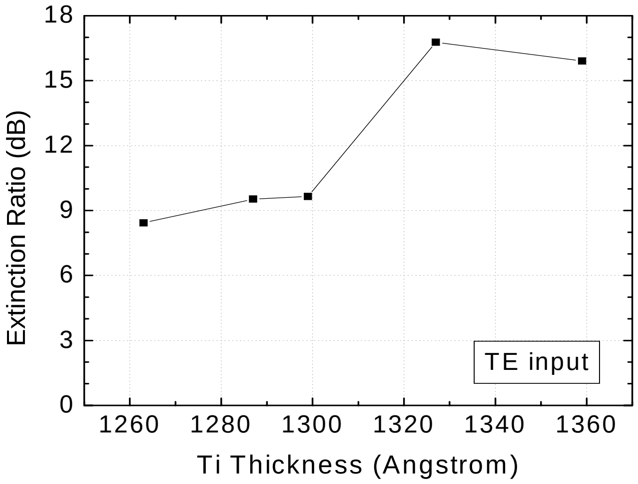

Figure 25. The ER of samples ks17, ks24, ks23, ks28, and ks29 with corresponding Ti film thicknesses of 1263Å, 1287Å, 1299Å, 1327Å, and 1359Å all diffused at 1055°C for 9 hours for the TE-polarized input.

These three figures indicate that the initial Ti film thicknesses along with diffusion temperature and time are controlling factors for achieving high extinction ratios. For a thin Ti film diffused at a low temperature the index difference between the two simultaneously excited modes (symmetric fundamental mode and asymmetric lowest-order mode) in the central region was not large enough to satisfy the phase conditions for acceptable polarization splitting, especially for the TE-polarized mode and that caused the low splitting ratios. With the thicker Ti film thickness (> 1300 Å) and the compatible high diffusion temperature, the ER of TE mode improved significantly as shown in Figure 25, and the waveguide maintained the single mode propagation. Extinction ratios of 16.8 dB and 20.5 dB for TE and TM modes, respectively was measured on sample ks28 and 15.9 dB and 24.8 dB for TE and TM modes was measured on sample ks29. The ER for various central interaction length $L_c$ on sample ks28 and ks29 are shown in Figure 26 and 27.

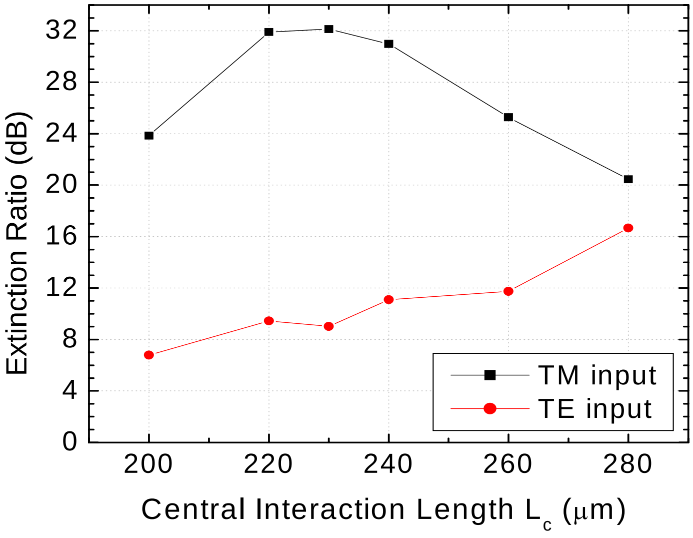

Figure 26. The ER of various central interaction length $L_c$ for TM- and TE-polarized inputs on sample ks28 with Ti film thickness of 1327 Å diffused at 1055°C for 9 hours.

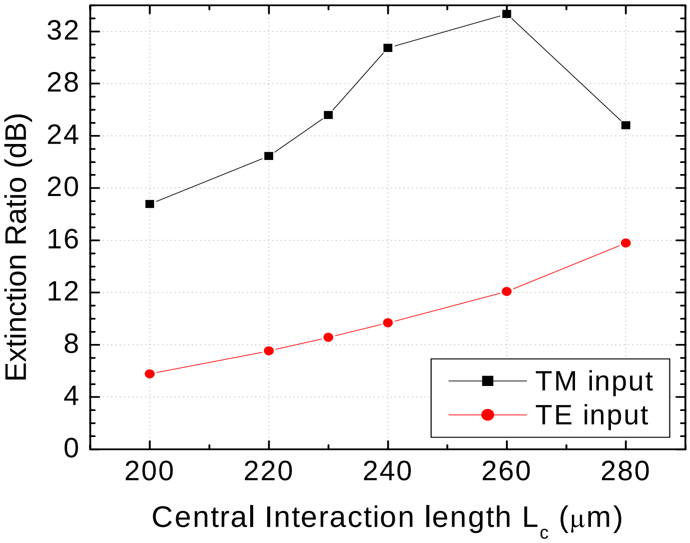

Figure 27. The ER of various central interaction length L$_c$ for TM- and TE-polarized inputs on sample ks29 with Ti film thickness of 1359 Å diffused at 1055°C for 9 hours.

The behaviors in Figure 26 and 27 suggest that the ER of TE and TM polarizations varies considerably with the interaction region length, the ER of the TM polarization is better than of the TE polarization, and the best extinction ratio for the TE polarization is obtained with the longest available central region length [35]. Figure 28 shows the ER variation with diffusion time at 1055°C tested with the splitter of 280 μm long interaction length on sample ks28 for TE and TM modes and it reveals the ER of both TM and TE modes degrades with longer diffusion time. Another sample ks25 with Ti film thickness of 1336 Å that was diffused at the same temperature of 1055°C but for a shorter diffusion time of 8 hours showed lower ER, and with additional diffusion time the ER of sample ks25 did not improve. Thus, it was concluded that a polarization beam splitter with more than 1300 Å Ti film thickness diffused at 1055°C for 9 hours would provide acceptable extinction ratios.

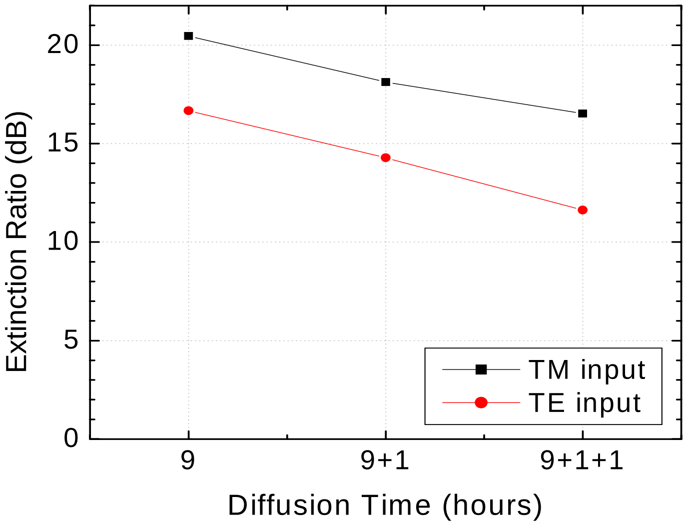

Figure 28. The ER with different diffusion time at 1055°C tested with the splitter of 280 μm long interaction length on sample ks28 for TE and TM modes.

## C. Tunable TE↔TM Polarization Mode Converters

Based on earlier analysis, a tunable TE↔TM polarization mode converter is a key element of an optical tunable filter and consists of three parts: a single-mode Ti-indiffused channel waveguide, one pair of electrodes, and a phase-matched periodic strain-induced index grating, as depicted in Figure 15. To evaluate the performance of a tunable TE↔TM polarization mode converter the test setup, illustrated in Figure 29, was used.

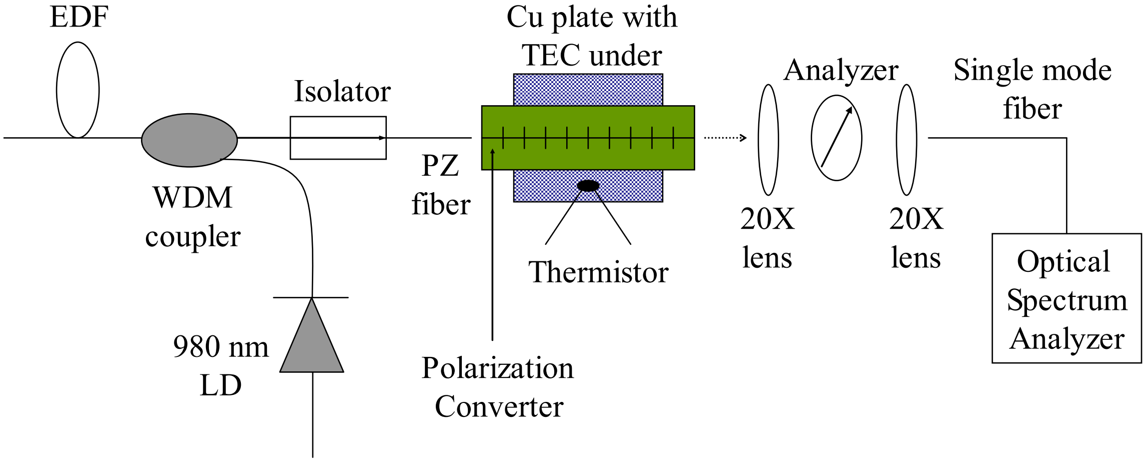

Figure 29. The test setup for a polarization mode converter.

To test wavelength selectivity and electrooptic tuning in the polarization mode converter, a broadband source is needed. The Amplified Spontaneous Emission (ASE) light from an Erbium-Doped Fiber Amplifier (EDFA) in the 1.55 μm wavelength regime was used as a broadband light source. The broadband ASE source was assembled with a backward pumping configuration, as illustrated in Figure 29. A 5m long erbium-doped fiber (EDF) was pumped by a 980 nm laser diode (LD) (SDL Optics Inc. Model: SDLO-2400-090) through a 980/1550 nm WDM coupler. An optical isolator (Kaifa Technology, Model: IS-A-55-B-A-11) with more than 38 dB isolation was placed at the output of the coupler to prevent self-oscillation (lasing). The broadband ASE light was butt coupled into a flat-polished end-edge of a channel waveguide through a single mode polarizing fiber (PZ fiber) which can be rotated to select either TE or TM polarization. The polarization extinction ratio > 35 dB was achieved for both TE- and TM-polarized inputs. The test sample placed on a Cu plate with a thermoelectric cooler (TEC) below it was mounted on a high resolution x-y-z translation stage. The thermoelectric cooler was used to control the substrate temperature for thermal tuning. A thermistor (Omega Model: 44030) placed on the Cu plate was used to measure the temperature. The output light was collimated by a 20× objective lens and passed through a polarization analyzer to select the output polarization for characterization. A second 20× objective lens was used to focus and couple the light into a cleaved single mode fiber and monitor the output spectrum on an Optical Spectrum Analyzer (OSA) (Anritsu, Model MS9710C). The ASE output power as a function of the LD pump current is shown in Figure 30. An ASE power of 1 mw at a pump current of 75 mA was coupled into the waveguide. The spectrum of ASE light is shown in Figure 31.

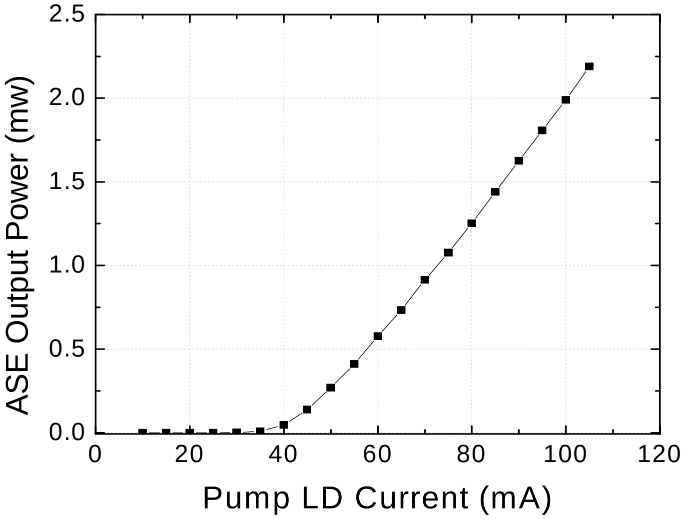

Figure 30. ASE output power variation with the pump LD current.

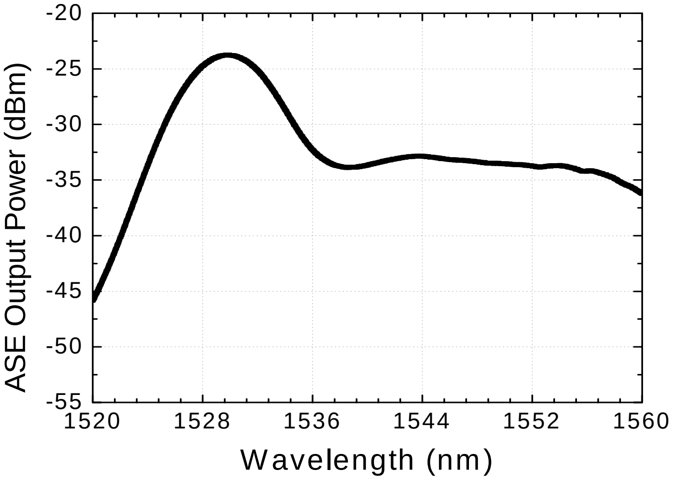

Figure 31. ASE output spectrum at the pump LD current of 75mA.

To characterize the polarization mode converter, the polarization state of the input light has to be either TE or TM polarization. From the analysis of a converter the strain-induced index change $\Delta n_5$, given in equation (74), is responsible for the polarization conversion and it depends on the thickness of $SiO_2$ film and the elevated temperature during the $SiO_2$ deposition. It was found that converters with a $SiO_2$ film thickness between 1.40 ~ 1.60 μm deposited at 360°C provide the best conversion. The output spectra of a mode converter with a total of 765 strain-induced index gratings of a 21 μm spatial period on sample k77 for TE- and TM-polarized inputs are shown in Figure 32. The 7 μm wide channel waveguide of sample k77 was produced from a 1210 Å thick Ti film diffused at 1050°C for 12 hours, and the strain inducing pads were produced from a 1.60 μm thick $SiO_2$ film deposited at 360°C. Figures 32(b) and (d) show the TM→TE conversion and TE→TM conversion, respectively, and both reveal very comparable converted profiles at the phase-matched wavelength of 1530.88 nm with a -3 dB bandwidth (FWHM) of 1.56 nm at 30°C substrate temperature. The -3dB bandwidth is in close agreement with the expected value from $\Delta\lambda = 0.8(\lambda_o / N)$ with $\lambda_o$ = 1530.88 nm and N = 765.

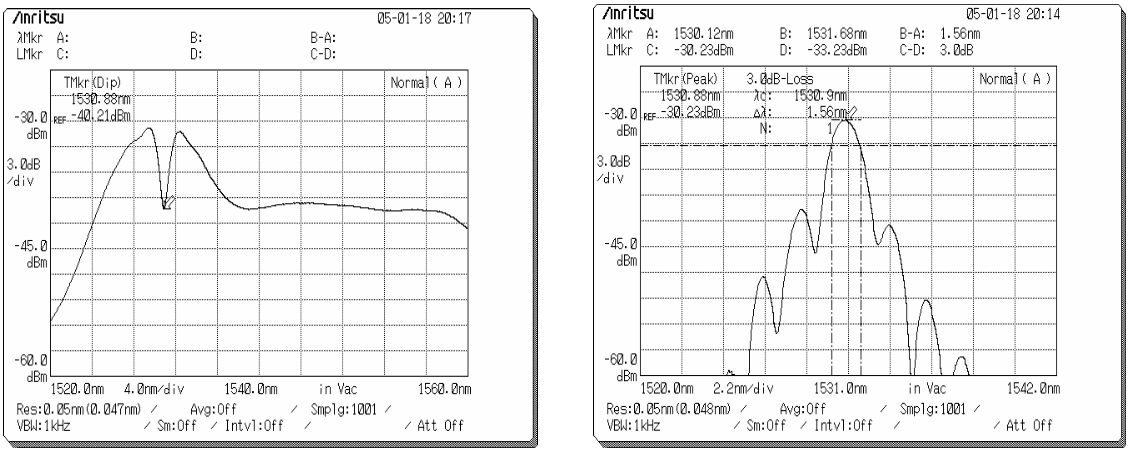

(a) Unconverted TM mode output (b) TM→TE conversion

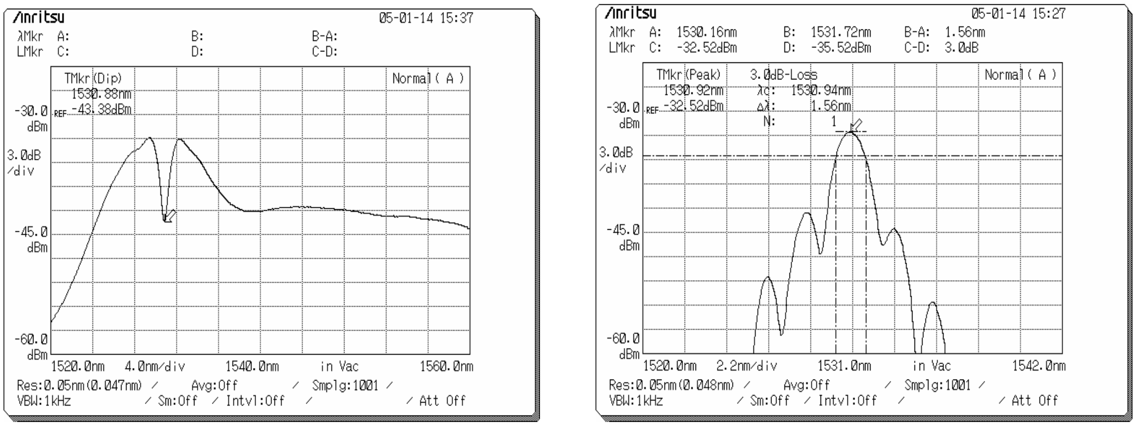

(c) Unconverted TE mode output (d) TE→TM conversion

Figure 32. Output spectra of a polarization mode converter for TE and TM polarizations on sample k77 at 30ºC substrate temperature. (a) and (b) are for TM-polarized input. (c) and (d) are for TE-polarized input.

The simulated conversion profiles with various number of grating N predicted from equation (79) are shown in Figure 33, and the experimental results of corresponding number of gratings with the -3 dB bandwidth measurements are illustrated in Figure 34. The data in Figures 34(a) and (b) are for mode converters with 300 and 500 gratings of 21 μm spatial periods fabricated on 7 μm wide waveguides (sample k106) with a 1.45 μm thick $SiO_2$ film, and the 765 gratings with 21 μm spatial periods (Figure 34(c)) were produced on sample k77. Figure 33 and 34 show the close agreement.

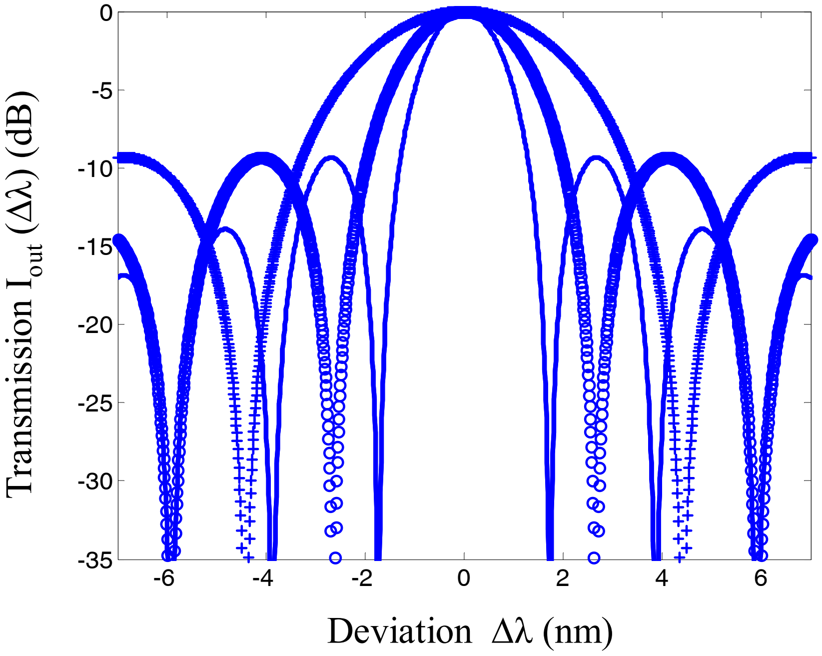

Figure 33. Normalized converted power profiles with various number N of uniform gratings. N = 300 (o), 500 (+), and 765 (—).

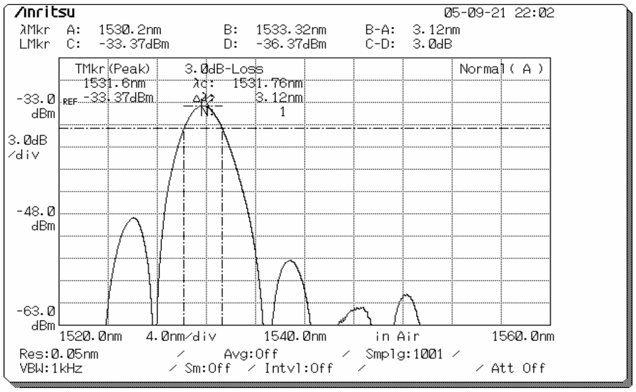

(a) N = 300, FWHM = 3.12nm.

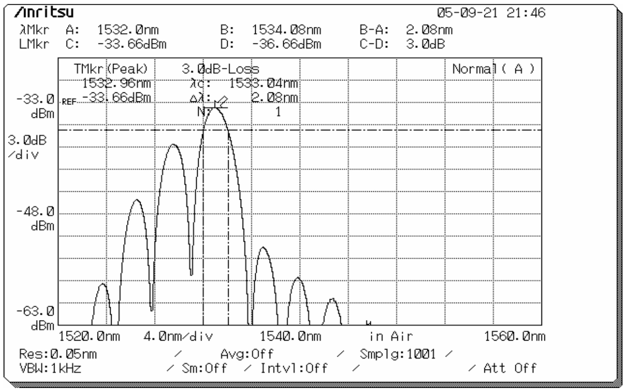

(b) N = 500, FWHM = 2.08nm.

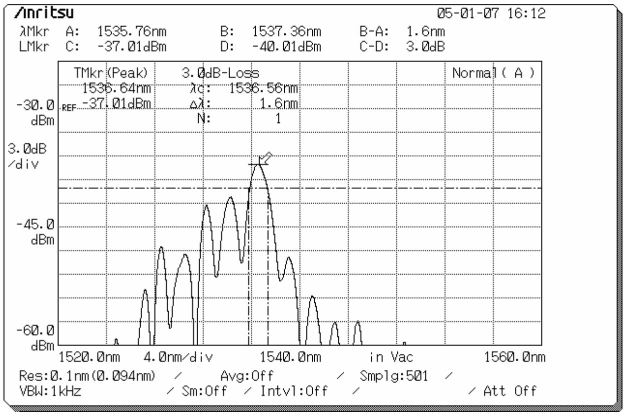

(c) N = 765, FWHM = 1.60nm.

Figure 34. The output spectra of converters with various grating number N for the TM-polarized input at 23ºC substrate temperature without applying a DC voltage.

Conversion efficiency, as defined in equations (81) and (82), is another feature to evaluate the performance of a mode converter. The ideal conversion efficiency is equal to one. Figure 35 shows the measured conversion efficiency as a function of the wavelength for both TE- and TM-polarized inputs tested with a 765-grating mode converter on sample k77 at 23°C. It reveals 98.2% conversion efficiency at the phase-matched wavelength of 1536.64 nm, and corresponds to a birefringence value Δn of 0.0732.

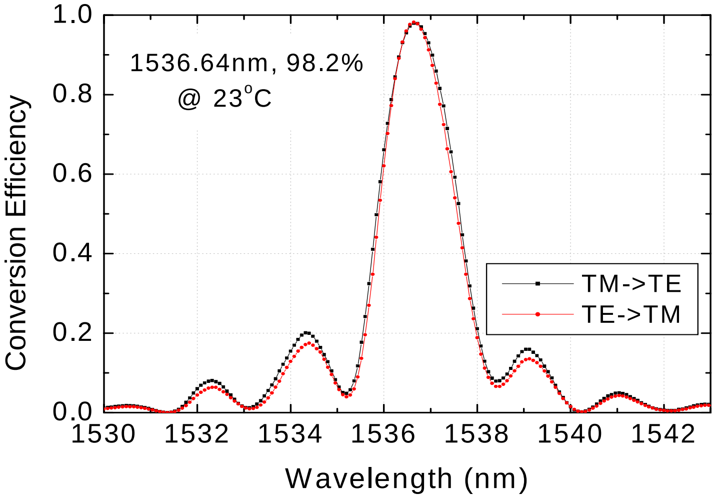

Figure 35. Conversion efficiency as a function of wavelength tested on sample k77 at 23°C for both TE- and TM-polarized inputs.

Since the refractive indices in $LiNbO_3$ vary with the temperature ($d(n_e-n_o)/dT$ ~ -2.9091×10-5 /°C at wavelength 1.40 μm) [36], from $\lambda_o = \Delta n \Lambda$ with fixed $\Lambda$ = 21 μm the converted wavelength can be tuned by changing the substrate temperature via a thermoelectric cooler. With thermal tuning, the phase-matched wavelength shifted from

1530.88 nm at 30°C to 1542.72 nm at 16°C on sample k77 as shown in Figure 36, indicating a thermal tuning rate of -0.846 nm/°C.

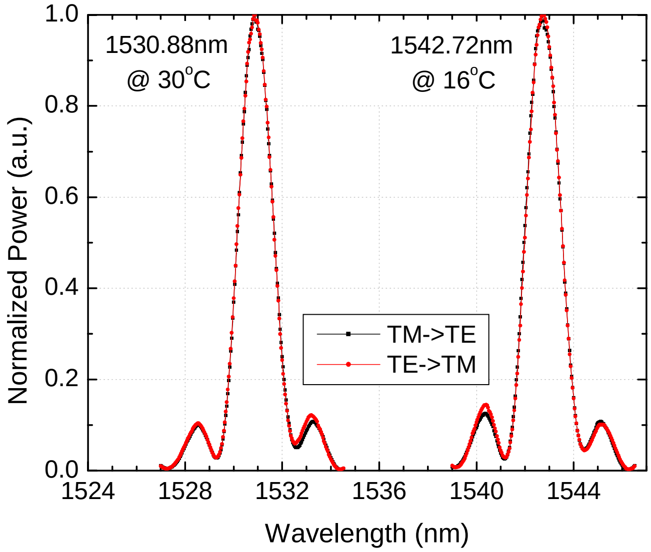

Figure 36. Normalized converted power as a function of wavelength for both TE- and TM-polarized inputs tested on sample k77 with thermal tuning.

Another tuning mechanism is using the electrooptic effect to change the refractive indices via an applied DC voltage on the substrate along the optic axis. Figure 37 shows the linear tuning behavior of the converted peak wavelength on sample k77 for TE- and TM-polarized inputs. The wavelength shifted by 9.76 nm with a DC voltage tuning from -100 V to +60 V corresponding to a tuning rate of 0.061 nm/V with the electrode gap of 17 μm. Assuming the overlap factors between the applied electric field and the optical field for TE and TM polarizations are equal, $\Gamma_{TE} = \Gamma_{TM}$, the overlap factor is calculated from equation (85) as 0.47, for the electrode gap of 17 μm.

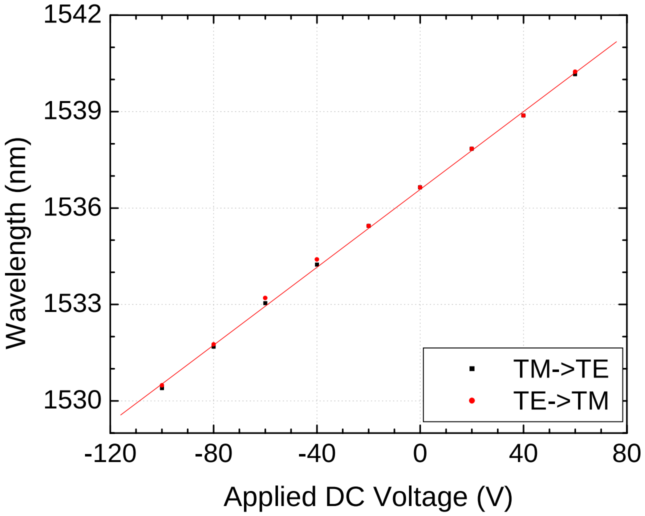

Figure 37. Electrooptic tuning of the center wavelength for TE- and TM-polarized inputs with the electrode gap of 17 μm tested on sample k77 at 23°C.

### D. Electrooptically Tunable Add Drop Filters

A tunable add/drop filter has two main elements: a polarization beam splitter and a tunable TE↔TM polarization mode converter. The performance of both has been optimized to produce high extinction ratio for the polarization beam splitter, and high conversion efficiency with a narrow -3 dB bandwidth (FWHM) for the polarization mode converter. Using the optimized fabrication parameters, first Ti-indiffused waveguides including the input and output single mode channel waveguides, the two polarization beam splitters, and the two single mode channel waveguides of polarization mode converters were integrated on an x-cut y-propagating $LiNbO_3$ substrate, as illustrated in Figure 38. After both edges were finely polished for fiber coupling, the overall extinction ratio (ER) was measured using the same test arrangement shown in

Figure 22. The test results and analysis are discussed later in this section. Then electrode pads made with Cr/Au/Ti were produced on the surface along the sides of the polarization mode converter regions for electrooptic tuning. Finally 765 periodic strain-induced index gratings were formed using a $SiO_2$ film on top of the electrode pads for TE↔TM mode conversion. The output profile of a complete tunable add/drop filter was examined using the setup shown in Figure 39.

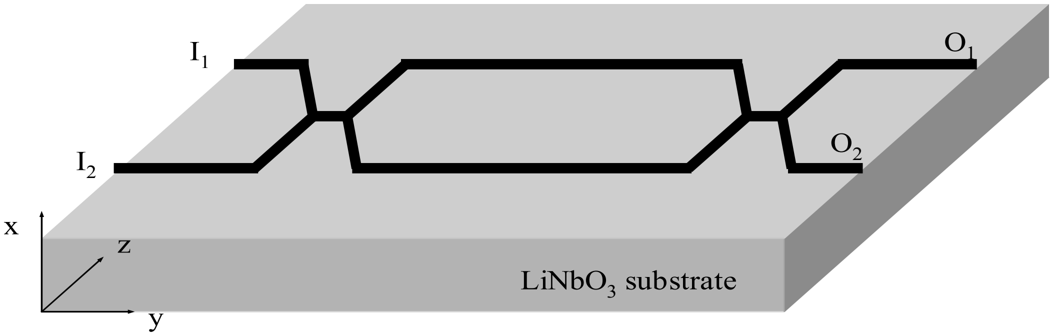

Figure 38. The first layer of Ti-indiffused waveguides for a tunable add/drop filter.

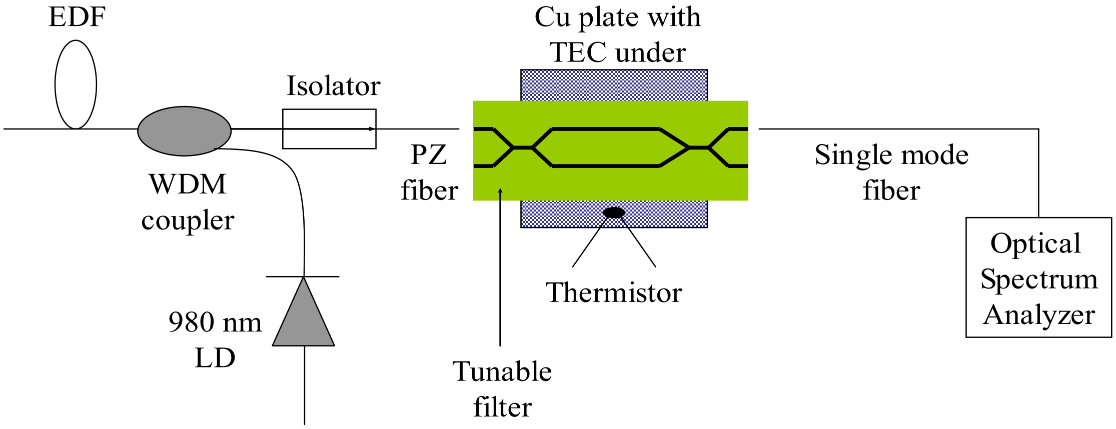

Figure 39. The test setup for a tunable add/drop filter.

The setup is similar to that of Figure 29. The broadband ASE light was butted coupled into the input port of a tunable filter through a single mode polarizing fiber (PZ fiber). The tested filter device was places on an x-y-z stage. The output spectra of the express port ($O_1$) and the drop port ($O_2$) were viewed with an optical spectrum analyzer (OSA). The observed characteristics of tunable add/drop filters are presented next.

D-1. Overall extinction ratio

After the first layer of Ti-indiffused waveguides formation, as illustrated in Figure 38, the overall extinction ratio (ER) of the filter device was tested before forming the second and third layers. The configuration could be treated as two polarization beam splitters jointed together. For either input state of polarization, signals entering into the input port $I_1$ should ideally emerge from the express port $O_1$ of the interferometer configuration, and the overall extinction ratio, R, could be evaluated using

$$\begin{aligned} R_{TM\,input} &= -10\log\left(\frac{\left(P_{o_2}\right)_{TM}}{\left(P_{o_1}\right)_{TM}+\left(P_{o_2}\right)_{TM}}\right) \\ R_{TE\,input} &= -10\log\left(\frac{\left(P_{o_2}\right)_{TE}}{\left(P_{o_1}\right)_{TE}+\left(P_{o_2}\right)_{TE}}\right) \end{aligned} . \qquad (94)$$

The interferometer configuration was tested with the setup shown in Figure 22. The overall ER obtained with different initial Ti film thicknesses for TE and TM inputs is shown in Figures 40 and 41 for devices which had 280 μm long central interaction length. The results for samples k211, k209, k208, k210, and M6 with corresponding Ti thicknesses of 1166 Å, 1190 Å, 1208 Å, 1226 Å, and 1250 Å are shown in Figure 40.

(Appendix 16 for device details) Samples k209, k208, and k210 were diffused at 1050°C for 11 hours. Samples k211 and M6 were diffused at 1035°C for 11 hours and at 1060°C for 10 hours, respectively. Compared with the ER of a single splitter, the thinner Ti film produced much worse overall ER. Figure 41 reveals the overall ER of samples K17, K11, K14, K13, and K10 with thicker Ti film of 1347 Å, 1350 Å, 1360 Å, 1362 Å, and 1395 Å, respectively. (Appendix 16 for device details) Both figures indicate the opening window of the Ti film thickness for achieving the comparable overall ER for TE and TM inputs is very limited. It gives a strict tolerance range of fabrication parameters to attain the high and comparable overall ER for both polarizations. The highest and most comparable overall ER from the tested samples are 16.0 dB for the TE input and 18.8 dB for the TM input, and were obtained for 280 µm central interaction region length on sample K11.

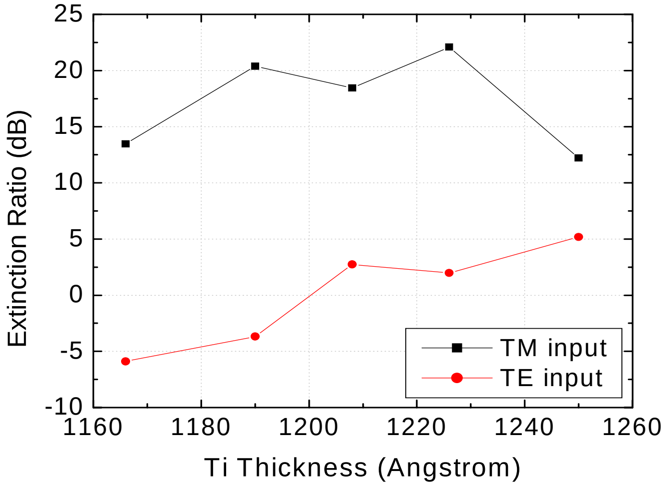

Figure 40. The overall ER variation with Ti film thickness tested on filter device #6C of different samples, k211, k209, k208, k210, and M6.

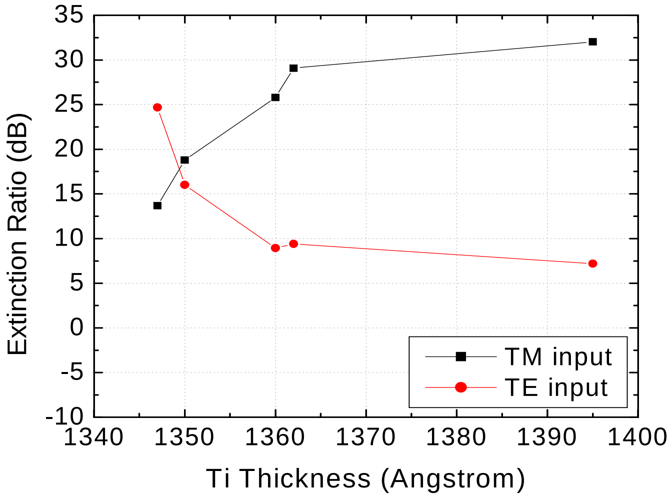

Figure 41. The overall ER variation with Ti film thickness tested on filter device #6C of different samples, K17, K11, K14, K13, and K10, all diffused at 1055°C for 9 hours.

Figure 42 shows the overall ER as a function of central interaction region length $L_c$ for sample K11 produced from a 1350 Å thick and 7 μm wide Ti strip at a diffusion temperature of 1055°C for 9 hours. According to the phase conditions given in equation (70), three factors: 1) propagation constant difference $\Delta\beta$ between fundamental mode and asymmetric mode, 2) central interaction length $L_c$, and 3) generated phase difference $\Delta\varphi(\alpha)$ in the transition region need to be matched well to produce high splitting ratio. $\Delta\beta$ is strongly related to fabrication parameters including initial Ti film thickness, diffusion temperature, and diffusion time. $\Delta\varphi(\alpha)$ is affected by the confinement of mode profiles and the opening angle of $\alpha$. Optimization of these three factors is needed to produce polarization beam splitters with high extinction ratio for the desired filter application.

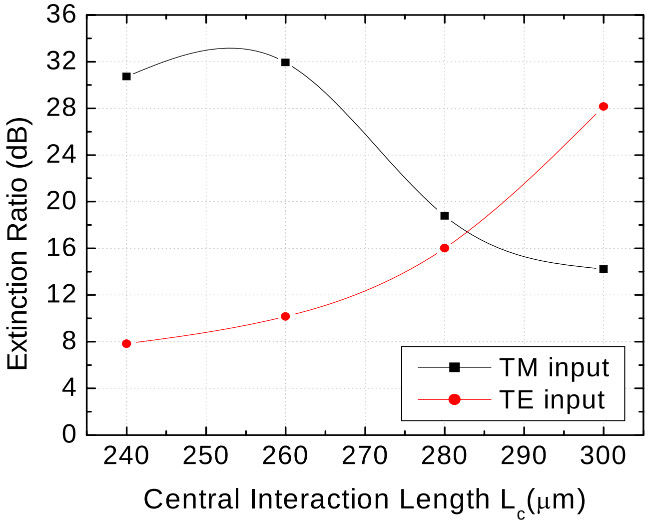

Figure 42. The overall ER as a function of central interaction length $L_c$ on tested sample K11 with Ti film thickness of 1350 Å diffused at 1055°C for 9 hours.

D-2. Spectral characteristics

Once the overall extinction ratio was measured, the second layer of electrode pads and third layer of 765 uniform index gratings were fabricated on top of the substrate and a tunable add/drop filter was produced, as shown in Figure 16. The spectral characteristics were examined with the arrangement given in Figure 39. Figure 43 shows the output spectra of the express port $O_1$ and the drop port $O_2$ for the filter which has 280 μm central interaction length on sample K11 at 25.5°C substrate temperature without applying a DC voltage. Figure 43(b) indicates the peak wavelength of the drop port is at 1530.24 nm with a -3 dB bandwidth (FWHM) of 1.56 nm in close agreement with the expected value from $\Delta\lambda = 0.8(\lambda_o/N)$ with $\lambda_o = 1530.24$ nm and N = 765.

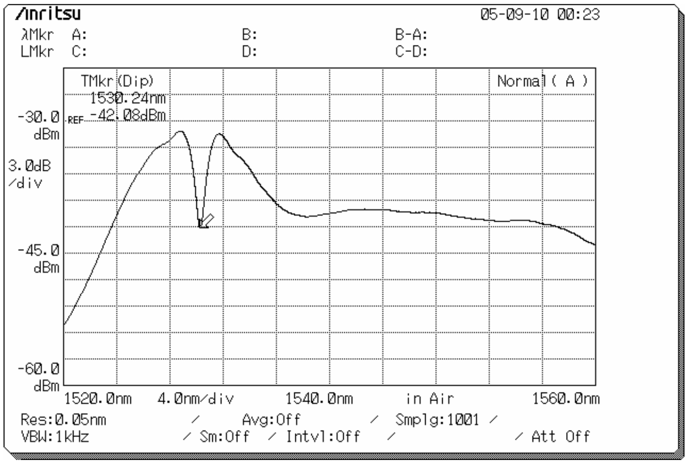

(a) Spectrum of express port

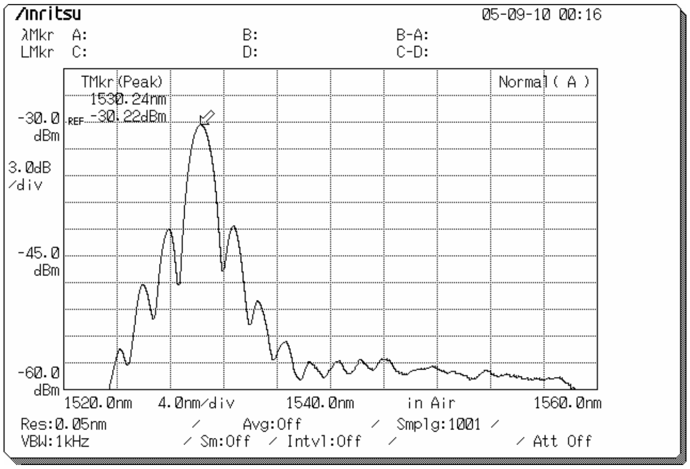

(b) Spectrum of drop port

Figure 43. Output spectra of the filter device #6C on sample K11 at 25.5ºC substrate temperature for the TM-polarized input without applying a DC voltage.

To evaluate the transmission performance of the add port $I_2$ the transmitted profile of at the express port $O_1$ was examined by coupling the ASE light into the add port $I_2$ at 25.5°C substrate temperature without applying voltages. Figure 44 compares the performance of the drop port $O_2$ and the express port $O_1$. They reveal nearly identical spectra with a -3 dB bandwidth of 1.56 nm at the same phase match wavelength of ~ 1530 nm, and the nearest sidelobe of both is about 12 dB below the central main peak, which is somewhat better than the theoretical value of ~ 9.5 dB for uniform gratings.

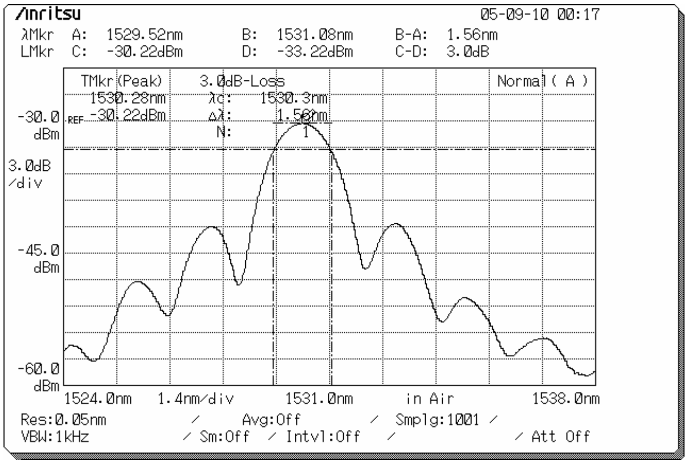

(a) Output spectrum at drop port $O_2$

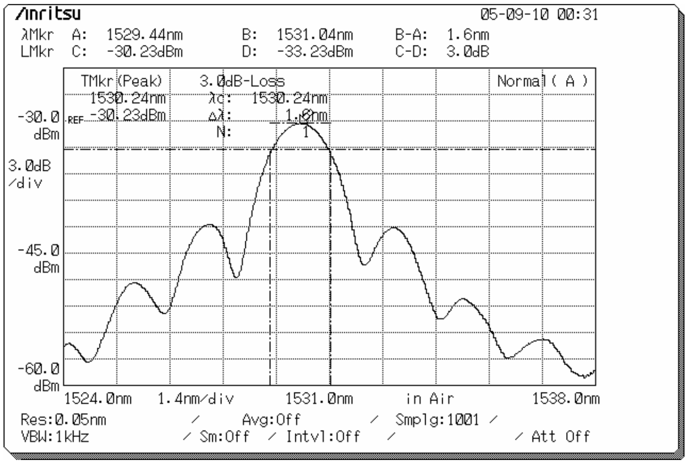

(b) Transmitted spectrum at express port $O_1$

Figure 44. Comparison of output spectra between the drop port and the express port tested on filter device #6C of sample K11 at 25.5°C for the TM-polarized input without applying a DC voltage.

### D-3. Temperature dependence

Since the refractive index in a $LiNbO_3$ crystal depends on the temperature [36], the phase-matched condition, $\Lambda = \lambda_o/\Delta n$, could be adjusted by thermal tuning the substrate temperature $T_s$ via a thermoelectric cooler. Figure 45 shows the normalized drop port spectrum of the filter with 280 μm interaction region length on sample K11 at two substrate temperature values for the TM-polarized input. The phase-matched wavelength shifted from 1526.96 nm at 29°C to 1539.60 nm at 15°C, indicating a thermal tuning rate of -0.903 nm/°C.

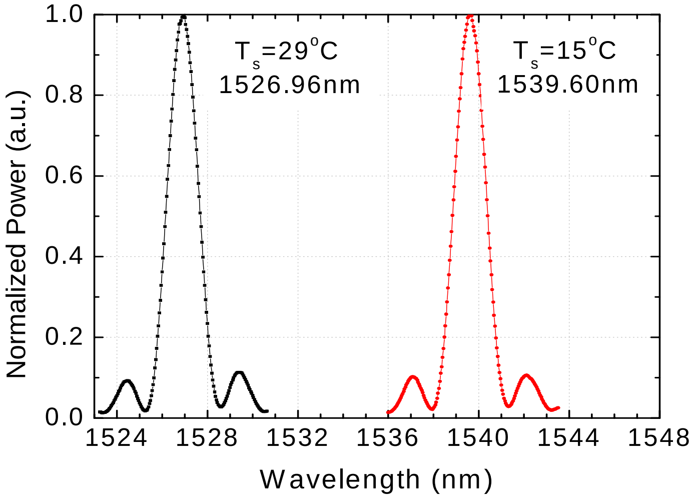

Figure 45. Normalized thermal tuning performance of filter device #6C on sample K11 for the TM-polarized input without applying a DC voltage.

### D-4. Electrooptic tuning

Another tuning mechanism is by applying a DC voltage on the $LiNbO_3$ substrate along optic axis to induce refractive index changes via the linear electrooptic effect.

Figure 46 shows the phase-matched wavelength shift of the filter for two devices, each of 280 µm interaction region length (#6C and #14C, in Appendix 14), on sample K11 for TM-polarized input. Filter devices #6C and #14C correspond to the electrode gap of 17 µm and 13 µm, respectively and reveal maximum tuning range of 11.36 nm and 14.08 nm achieved by applying a DC voltage ranging from -80 V to +80 V. The tuning range is mainly limited by the electric field breakdown of $LiNbO_3$ crystal (nearly 10 V/ µm) [13], and also depends on the gap between electrode pads, and the quality of electrode metal deposition. The narrower electrode gap provides a larger tuning range. The electrooptic tuning rate is 0.07 nm/V for the 17 µm electrode gap and 0.086 nm/V for the 13 µm electrode gap.

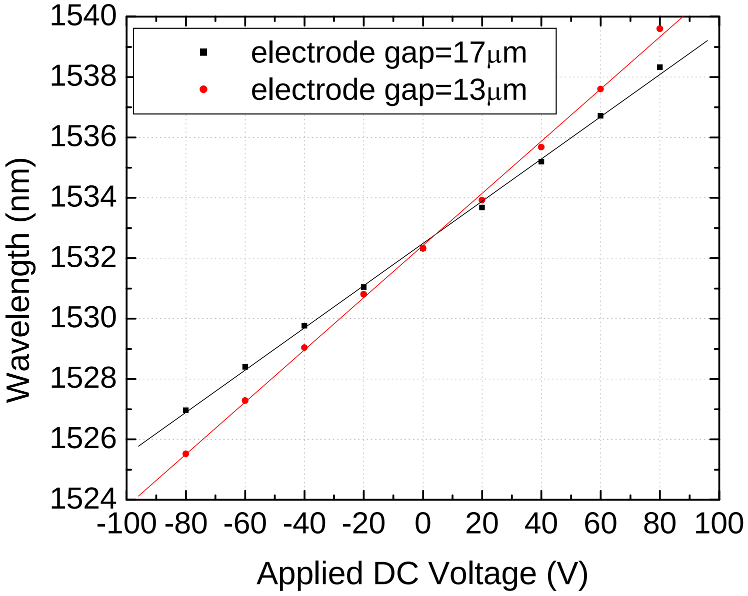

Figure 46. Electrooptic tuning performance of filter devices #6C and #14C on sample K11 at 23°C for the TM-polarized input.

Figure 47 shows the normalized spectral response of the filter with 280 μm interaction region length (device #6C in Appendix 14) with applying DC voltages from -80 V to +80 V on sample K11 at 23°C for TM-polarized input, and it gives tuning range of 11.36 nm for the 17 μm electrode gap.

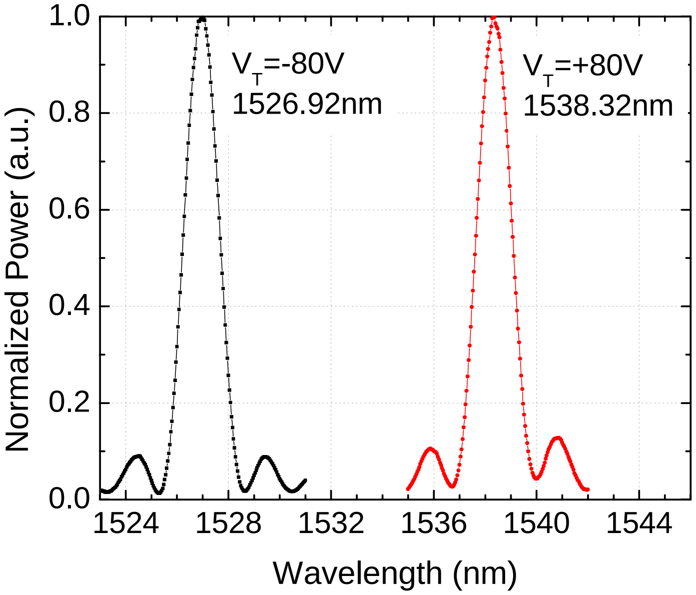

Figure 47. Normalized spectral characteristics of electrooptic tuning for the filter device #6C on sample K11 at 23°C for the TM-polarized input.

Two different tuning mechanism have been demonstrated, thermal tuning and electrooptic tuning, although thermal tuning can provide wider tuning range, it requires longer time to stabilize, thus it is slow. The advantage of electrooptic tuning is in its rapid tuning response.

D-5. Polarization dependence

The polarization dependence of the transmitted spectra was also examined on the same filter device with TE-polarized and TM-polarized inputs, individually. Figure 48 shows the drop port performance of the filter device #6C on sample K11 at 25.5°C without applying a DC voltage for the TE-polarized input.

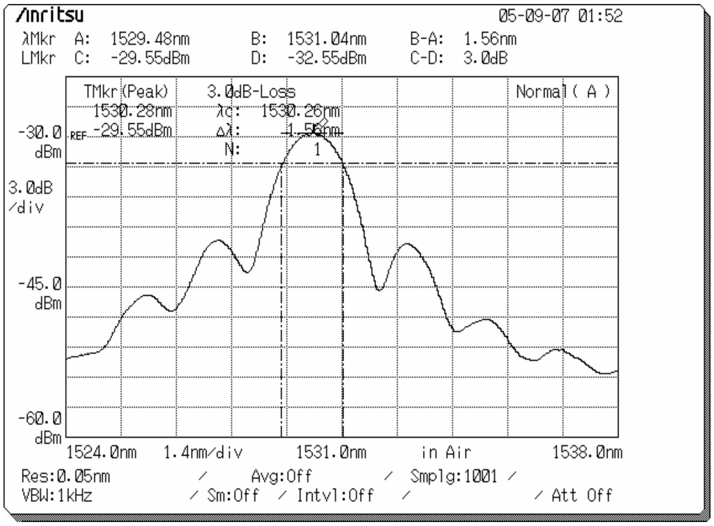

```
05-09-07 01:52
λMkr  A:  1529.48nm      B:  1531.04nm     B-A:  1.56nm
LMkr  C:  -29.55dBm      D:  -32.55dBm     C-D:  3.0dB
TMkr (Peak)        3.0dB-Loss
  1530.28nm          λc:  1530.26nm
  -29.55dBm          Δλ:     1.56nm
                     N:       1
Normal ( A )
Res:0.05nm       /    Avg:Off       /  Smplg:1001 /
VBW:1kHz        / Sm:Off  / Intvl:Off   /            / Att Off
```

Figure 48. The drop port performance of the filter device #6C on sample K11 at 25.5°C without applying a DC voltage for the TE-polarized input.

Compared with Figure 44(a), it indicates close spectral characteristics with a -3 dB bandwidth (FWHM) of 1.56 nm at peak wavelength 1530.24 nm. For the TE-polarized input the nearest sidelobe is slightly higher than for the TM-polarized input; and this maybe because the overall extinction ratio of the TM-polarized input is somewhat better than that of the TE-polarized input. The fiber-to-fiber insertion loss at wavelength 1530.24 nm is 5.7 dB and 6.3 dB for TE- and TM-polarized input, respectively, on the 62 mm long filter device. Figure 49 shows the electrooptic tuning performance of filter devices #6C and #14C with corresponding electrode gaps of 17 µm and 13 µm on sample K11 at 23°C for both polarizations, and Figure 50 shows the normalized thermal tuning characteristics of the drop port tested with the filter device #6C of sample K11 for both TE- and TM-polarized inputs without applying a DC voltage. The results shown in those figures confirm that the tunable add/drop filter is polarization independent.

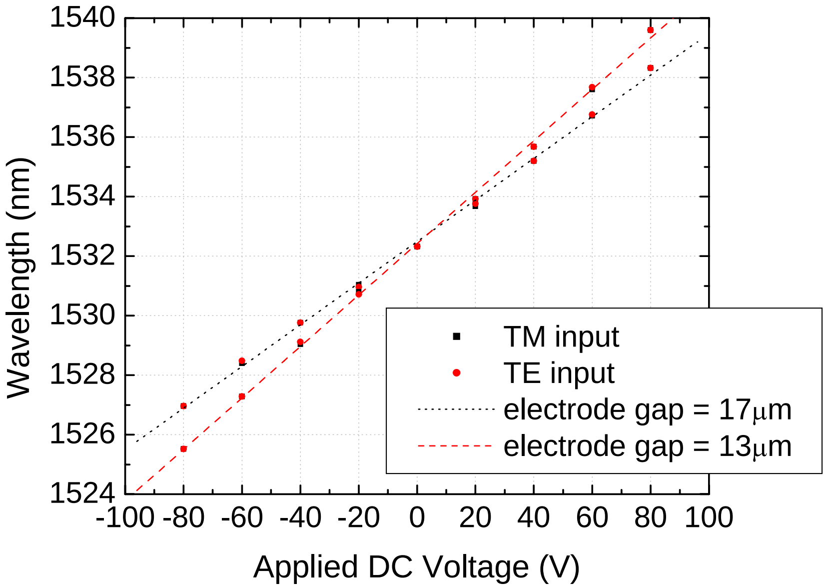

Figure 49. Electrooptic tuning performance of the filter device #6C and #14C on sample K11 at 23°C for TE- and TM-polarized inputs.

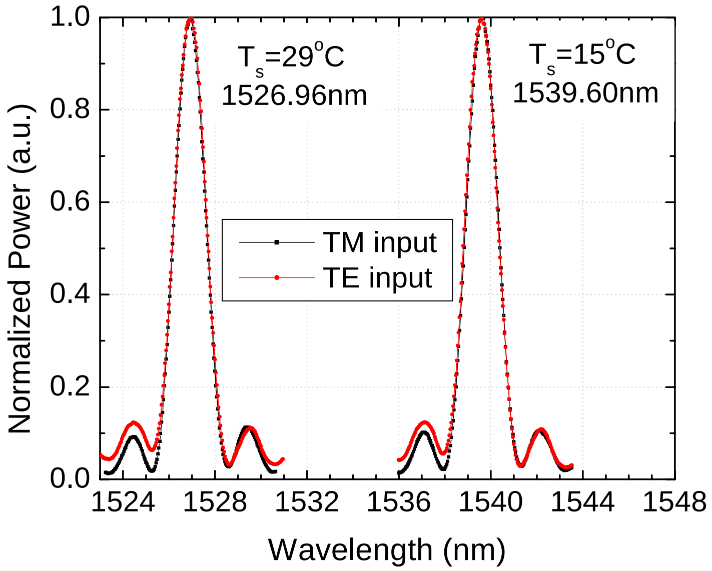

Figure 50. Normalized thermal tuning characteristics of the filter device #6C on sample K11 without applying a DC voltage for TE- and TM-polarized inputs.

# CHAPTER VI

# CONCLUSION

To satisfy the demands of fast tuning speed and an increased number of communication channels for dense WDM networks, a polarization independent electrooptic add/drop tunable filter on a $LiNbO_3$ substrate with a narrow -3 dB bandwidth (FWHM) of 1.56 nm operating in the 1.55 μm wavelength regime has been developed. The performance of the filter is based on passive polarization beam splitters and strain-induced phase-matched polarization mode converters. The principle of operation of a tunable filter and its key elements were discussed.

Channel waveguides of various widths and fabrication parameters were fabricated using Ti indiffusion technology on x-cut y-propagating $LiNbO_3$ substrates. A 7 μm wide channel waveguide with Ti film thickness of 1350 Å diffused at 1055°C for 9 hours indicated single mode propagation and fiber-to-fiber insertion loss of 2.99 dB and 2.60 dB for TE- and TM-polarized inputs, respectively, on a 62 mm long substrate.

Polarization beam splitters with an opening angle of 0.55° and a central interaction region length $L_c$ ranging from 200 μm to 280 μm were produced on x-cut y-propagating $LiNbO_3$ substrates with different fabrication parameters. Extinction ratios of 16.8 dB for TE and 20.5 dB for TM were measured on the 280 μm long interaction region length for a polarization splitter produced with Ti film thickness of 1327 Å diffused at 1055°C for 9 hours in wet ambient. To satisfy the phase conditions for both polarizations and produce high extinction ratio splitters, all fabrication parameters and the interaction length $L_c$ must be tightly controlled with strict tolerances.

Tunable TE↔TM polarization mode converters with uniform strain-induced index gratings made from a $SiO_2$ film have been produced and tested. The results confirmed that the -3 dB spectral bandwidth depends on the total number of index gratings. A polarization mode converter with a 765 strip index grating and a spatial period of 21 μm made from a 1.60 μm thick $SiO_2$ strain film produced a conversion efficiency of 98.2 % and a -3 dB bandwidth of 1.56 nm at the phase-matched wavelength of 1536.64 nm at the room temperature for both TE and TM input polarizations. Thermal tuning was used to shift the peak wavelength, and a thermal tuning rate of -0.846 nm/°C was achieved. Electrooptic tuning was also demonstrated to shift the phase-matched peak wavelength by 9.76 nm with voltage ranging from -100 V to +60 V and revealed an electrooptic tuning rate of 0.061 nm/V for an electrode gap of 17 μm.

A polarization independent electrooptic add/drop tunable filter was produced by the same process as the tunable TE↔TM polarization mode converter. The phase-matched wavelength at 1530.24 nm was directed towards the drop port at a 25.5°C substrate temperature. The transmission performance of the add port was also evaluated at that temperature and showed spectral characteristics very close to that of the drop port. Both reveal a -3 dB bandwidth of 1.56 μm and nearest sidelobes about 12 dB below the center peak. The fiber-to-fiber insertion loss at 1530.24 nm wavelength was less than 6.3 dB for both polarizations, measured on a 62 mm long filter device. Thermal tuning was used to shift the peak wavelength from 1526.96 nm at 29°C to 1539.60 nm at 15°C giving a thermal tuning rate of -0.903 nm/°C. Another tuning mechanism based on the electrooptic effect was also demonstrated. A maximum tuning range of 14.08 nm was achieved with an electrode gap of 13 µm indicating an electrooptic tuning rate of 0.086 nm/V. Thermal tuning and electrooptic tuning were examined for both TE and TM input polarizations and showed very comparable results, confirming that the tunable filter is polarization independent.

# CHAPTER VII

# SUGGESTIONS FOR FUTURE WORK

According to the obtained results the tunable filter with polarization beam splitters, shows a very strict tolerance range of fabrication parameters to satisfy the phase requirements of a polarization beam splitter for both TE- and TM-polarized inputs, simultaneously. New designs of an electrooptic tunable filter using Mach-Zehnder configuration with relaxed beam-splitter requirements have been proposed by Dr. H. F Taylor and Dr. O. Eknoyan [37]. The new electrooptic tunable filter (EOTF) design is illustrated in Figure 51.

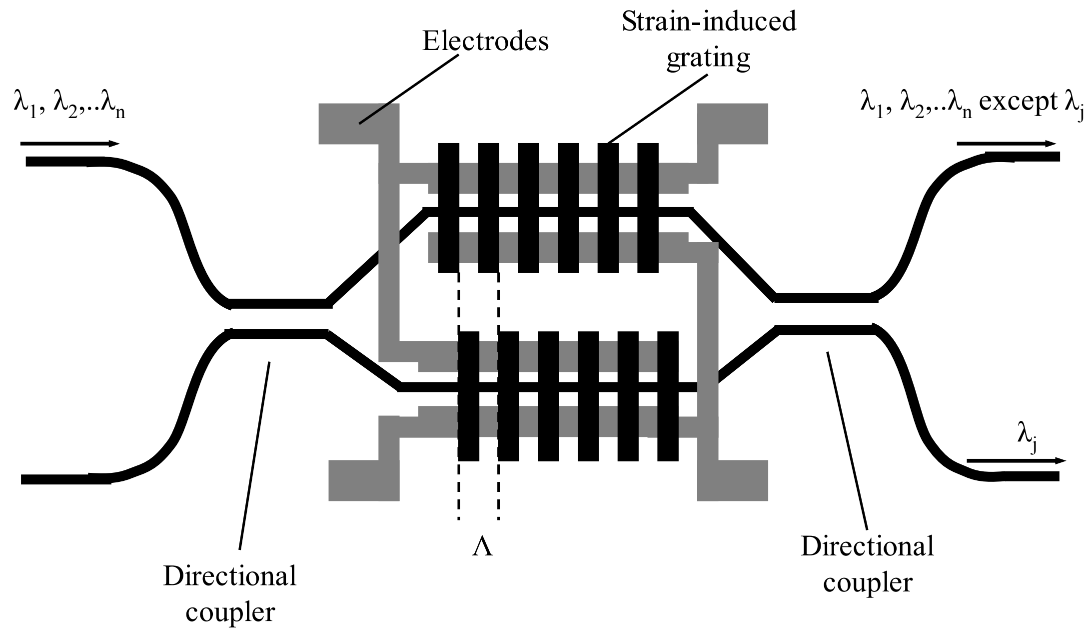

Figure 51. New design of an electrooptic tunable filter [37].

The new design differs from the investigated electrooptic tunable filter in this research study in following respects: 1) polarization beam splitters are not required and are replaced by finite gap directional couplers, 2) the optical path difference for the waveguides between two couplers for both TE and TM polarizations is a half-wavelength, or an odd integral multiple, and 3) the relative positions of the polarization coupling regions in two channel waveguides are displaced in the propagation direction by half of the spatial period of the perturbation responsible for the coupling. In this configuration, the directional couplers must satisfy one condition:

$$\left(f_{TE}\right)_{ii} + \left(f_{TM}\right)_{ii} = 1 \tag{95}$$

with i = 1 or 2, where $(f_p)_{ij}$ is the fraction of incident power at port i with the polarization p exiting at port j. In this configuration the coupling length, the waveguide width, and the opening angle are fixed, and only the separation gap is varied. By measuring $(f_{TE})_{ii}$ and $(f_{TM})_{ii}$ for various separation gaps, the condition of equation (95) can be satisfied. The new design relaxes the requirements for ideal polarization splitting and makes it easier to fabricate tunable add/drop wavelength filters.

# REFERENCES

[1] M. S. Borella, J. P. Jue, D. Banerjee, B. Ramamurthy, and B. Mukherjee, “Optical components for WDM lightwave networks,” *Proceedings of the IEEE*, vol. 85, no. 8, pp. 1274-1307, Aug. 1997.

[2] J. M. H. Elmirghani, and H. T. Mouftah, “Technologies and architectures for scalable dynamic dense WDM networks,” *IEEE Communications Magazine*, vol. 38, no. 2, pp. 58-66, Feb. 2000.

[3] H. Kobrinski, and K. W. Cheung, “Wavelength-tunable optical filters: applications and technologies,” *IEEE Communications Magazine*, vol. 27, no. 10, pp. 53-63, Oct. 1989.

[4] J. Stone and L. W. Stulz, “Pigtailed high-finesse tunable fiber Fabry-Perot interferometers with large, medium and small free spectral ranges,” *Electronics Letters*, vol. 23, no. 15, pp. 781-783, July 1987.

[5] A. Iocco, H. G. Limberger, and R. P. Salathe, “Bragg grating fast tunable filter,” *Electronics Letters*, vol. 33, no. 25, pp. 2147-2148, Dec. 1997.

[6] S. Suzuki, A. Himeno, and M. Ishii, “Integrated multichannel optical wavelength selective switches incorporating an arrayed-waveguide grating multiplexer and thermooptic switches,” *Journal of Lightwave Technology*, vol. 16, no. 4, pp. 650-655, Apr. 1998.

[7] E. C. Vail, M. S. Wu, G. S. Li, L. Eng, and C. J. Chang-Hasnain, “GaAs micromachined widely tunable Fabry Perot filters,” *Electronics Letters*, vol. 31, no.

3, pp. 228-229, Feb. 1995.

[8] L. Wooten, R. L. Stone, W. Miles, and E. M. Bradley, "Rapidly tunable narrowband wavelength filter using $LiNbO_3$ unbalanced Mach-Zehnder interferometers," *Journal of Lightwave Technology*, vol. 14, no. 11, pp. 2530-2536, Nov. 1996.

[9] F. Tian, Ch. Harizi, H. Herrmann, V. Reimann, R. Ricken, U. Rust, W. Sohler, F. Wehrmann, and S. Westenhofer, "Polarization-independent integrated optical, acoustically tunable double-stage wavelength filter in $LiNbO_3$," *Journal of Lightwave Technology*, vol. 12, no. 7, pp. 1192-1197, July 1994.

[10] P. Tang, O. Eknoyan, and H. F. Taylor, "Rapidly tunable optical add-drop multiplexer (OADM) using a static-strain-induced grating in $LiNbO_3$," *Journal of Lightwave Technology*, vol. 21, no. 1, pp. 236-245, Jan. 2003.

[11] D. Sadot and E. Boimovich, "Tunable optical filters for dense WDM networks," *IEEE Communications Magazine*, vol. 36, no. 12, pp. 50-55, Dec. 1998.

[12] Amnon Yariv, *Quantum Electronics*, 3rd edition. New York: John Wiley & Sons, 1989.

[13] H. Nishihara, M. Haruna, and T. Suhara, *Optical Integrated Circuits*. New York: McGraw-Hill, 1989.

[14] A. Yariv, and P. Yeh, *Optical Waves in Crystals*. New York: John Wiley & Sons, 1984.

[15] Z. Tang, "Study of utilizing static photoelastic effect in integrated optical devices," Ph.D. dissertation, Texas A&M University, Department of Electrical Engineering,

College Station, 1994.

[16] R. C. Alferness, “Efficient waveguide electro-optic TE↔TM mode converter/wavelength filter,” *Applied Physics Letters*, vol. 36, no. 7, pp. 513-515, April 1980.

[17] L. Bersiner, U. Hempelmann, and E. Strake, “Numerical analysis of passive integrated-optical polarization splitters: comparison of finite-element method and beam-propagation method results,” *Journal of Optical Society of America*, vol. 8, no. 2, pp. 422-433, Feb. 1991.

[18] H. Z. Hu, J. Chen, J. S. Yang, and F. Geng, “Structural auto-optimization of integrated optical directional coupler polarization splitters and reflectors,” *Journal of Lightwave Technology*, vol. 20, no. 5, pp. 868-872, May 2002.

[19] Y. S. Kim and R. T. Smith, “Thermal expansion of lithium tantalate and lithium niobate single crystals,” *Journal of Applied Physics*, vol. 40, no. 11, pp. 4637-4641, Oct. 1969.

[20] Y. S. Touloukian, R. D. Kirby, R. E. Taylor, and T. Y. R. Lee, *Thermophysical Properties of Matter*, New York: Plenum, 1977.

[21] O. Eknoyan, H. F. Taylor, J. M. Marx, Z. Tang, and R. R. Neurgaonkar, “Guided-wave electrooptic devices utilizing static strain induced effects in ferroelectrics,” *Ferroelectrics*, vol. 205, pp. 147-158, 1998.

[22] C. T. Wang, *Applied Elasticity*, New York: McGraw-Hill, 1953.

[23] P. S. Tang, “Polarization independent electrooptically tunable add drop filter in Ti:LiNbO$_3$ at 1.55 μm wavelength regime,” Ph.D. dissertation, Texas A&M

University, Department of Electrical Engineering, College Station, 2002.

[24] R. J. Pressley, *Handbook of Lasers with Selected Data on Optical Technology*, Cleveland: The Chemical Rubber CO., 1971.

[25] D. F. Nelson and R. M. Mikulyak, "Refractive indices of congruently melting lithium niobate," *Journal of Applied Physics*, vol. 45, no. 8, pp. 3688-3689, Aug. 1974.

[26] F. Heismann and R. C. Alferness, "Wavelength-tunable electrooptic polarization conversion in birefringent waveguides," *IEEE Journal of Quantum Electronics*, vol. QE-24, no. 1, pp. 83-93, Jan. 1988.

[27] R. C. Alferness and L. L. Buhl, "Long-wavelength Ti:$LiNbO_3$ waveguide electro-optic TE↔TM convertor," *Electronics Letters*, vol. 19, no. 1, pp. 40-41, Jan. 1983.

[28] R. C. Alferness, "Waveguide electrooptic modulators," *IEEE Transactions on Microwave Theory and Techniques*, vol. MTT-30, no. 8, pp. 1121-1137, Aug. 1982.

[29] R. V. Ramaswamy, S. I. Najafi, "Planar, buried, ion-exchanged glass waveguides: diffusion characteristics," *IEEE Journal of Quantum Electronics*, vol. QE-22, no. 6, pp. 883-891, June, 1986.

[30] R. J. Holmes and D. M. Smyth, "Titanium diffusion into $LiNbO_3$ as a function of stoichiometry," *Journal of Applied Physics*, vol. 55, no. 10, pp. 3531-3535, May 1984.

[31] L. McCaughan and E. J. Murphy, "Influence of temperature and initial titanium dimensions on fiber-Ti:$LiNbO_3$ waveguide insertion loss at $\lambda = 1.3$ μm," *IEEE Journal of Quantum Electronics*, vol. QE-19, no. 2, pp. 131-136, Feb. 1983.

[32] J. L. Jackel, V. Ramaswamy, and S. P. Lyman, “Elimination of out-diffused surface guiding in titanium-diffused $LiNbO_3$,” *Applied Physics Letters*, vol. 38, no. 7, pp. 509-511, 1981.

[33] P. G. Suchoski and R. V. Ramaswamy, “Minimum-mode-size low-loss $Ti:LiNbO_3$ channel waveguides for efficient modulator operation at 1.3 μm,” *IEEE Journal of Quantum Electronics*, vol. QE-23, no. 10, pp. 1673-1679, Oct. 1987.

[34] G. Eisenstein, S. K. Korotky, L. W. Stulz, J. J. Veselka, R. M. Jopson, and K. L. Hall, “Antireflection coatings on lithium niobate waveguide devices using electron beam evaporated yttrium oxide,” *Electronics Letters*, vol. 21, no. 9, pp. 363-364, April 1985.

[35] D. Yap, L. M. Johnson, and G. W. Pratt, Jr., “Passive $Ti:LiNbO_3$ channel waveguide TE-TM mode splitter,” *Applied Physics Letters*, vol. 44, no. 6, pp. 583-585, Mar. 1984.

[36] G. D. Boyd, W. L. Bond, and H. L. Carter, “Refractive index as a function of temperature in $LiNbO_3$,” *Journal of Applied Physics*, vol. 38, no. 4, pp. 1941-1943, Mar. 1967.

[37] H. F. Taylor and O. Eknoyan, “Guided wave acousto-optic and electro-optic tunable filter designs with relaxed beam-splitter requirements,” *Applied Optics*, vol. 39, no. 1, pp. 124-128, Jan. 2000.

# APPENDIX 1

# DICING WAFERS

1. Mount a blue tape to an o-ring and place a $LiNbO_3$ wafer on the tape.
2. **R** Turn on 5 knobs/switches for dicing: water valve behind the sink (yellow), air knob under bench (black), vacuum pump power switch under saw (silver), vacuum line switch under saw (black), water line valve under saw (yellow).
3. **R** Turn on saw power.
4. Select PROGRAM and program 300 was used. Confirm parameters.
5. Check two parameters of Height = 0.6 mm and Thickness = 1.2 mm for 1 mm thick wafer. Select PROGRAM again to finish setting.
6. **R** Turn on spindle and wait until indicated light was stabilized.
7. Select ZERO CHUCK. Be prepared to RESET if the blade cuts into chuck.
8. Place the wafer mount on the chuck, and select WAFER LOCK.
9. Select ALIGN. Align the wafer with crosshairs using controlling panels on right.
10. Press SINGLE CUT to start cutting.
11. Do a test run before cutting into the wafer.
12. When finished, select WAFER RELEASE.
13. Do steps marked **R** in reverse order to shut down system.
14. Take out diced substrates.

# APPENDIX 2

## SUBSTRATE CLEANING PROCEDURE

1. Brush a substrate gently with a Q-tip under soapy water.
2. Rinse thoroughly with D.I. water.
3. Sonicate in Acetone for 10 minutes.
4. Rinse with Methanol.
5. Sonicate in Methanol for 10 minutes.
6. Rinse with D.I. water.
7. Sonicate in soap water for 10 minutes.
8. Rinse with D.I. water.
9. Sonicate in D.I. for 10 minutes.
10. Rinse with Methanol.
11. Brush a substrate gently with a Q-tip under Methanol.
12. Blow dry with $N_2$.

# APPENDIX 3

# DC SPUTTERING PROCEDURE

1. Vent the chamber and load samples.
2. Close bell jar and turn on mechanical pump switch.
3. Turn on chamber roughing valve and wait until chamber pressure is below 50 μmHg.
4. Close roughing valve and open high vacuum valve all the way.
5. Wait until chamber pressure drops below $2 \times 10^{-6}$ Torr.
6. Turn on cooling system for thickness monitor and set the cooling temperature at 10°C.
7. Turn on Argon gas valve and set the flow rate at 140sccm.
8. Adjust high vacuum valve until Hastings vacuum gauge reads 20 μmHg.
9. Set parameters of thickness monitor.
10. Turn on power supply and select the red button.
11. Turn on the current dial slowly to 40 mA.
12. Pre-sputtering for 15 minutes.
13. Rotate to the sample position and start deposition.
14. After finish deposition, turn off the current dial, power supply, and Argon gas valve.
15. Reset the cooling temperature to 25°C and turn off the system.
16. Wait for more than two hours and take out samples.

# APPENDIX 4

# POSITIVE PHOTOLITHOGRAPHY PROCESS

1. Dehydrate samples at 135°C for 5 minutes.
2. Let samples cool down for 10 minutes.
3. Spin Clariant AZ 5214 photoresist at 5000 rpm for 30 seconds.
4. Soft bake samples at 99°C for 2 minutes.
5. Cool down samples for 10 minutes.
6. Expose samples under UV light with 11.0 $mw/cm^2$ power density for 3.75 seconds without filter.
7. Develop samples in a Shipley MF312:$H_2O$ = 1:1.2 solution for 55 seconds.
8. Rinse samples thoroughly with D.I. water.
9. Blow dry samples gently with $N_2$.

# APPENDIX 5

# POSITIVE PHOTOLITHOGRAPHY PROCESS ON $SiO_2$ FILM

1. Dehydrate samples with $SiO_2$ film at 135°C for 30 minutes.
2. Wait until samples cools down to room temperature.
3. Spin promotor first at 3000 rpm for 30 seconds for improving the adhesion between $SiO_2$ film and photoresist.
4. Spin Clariant AZ 5214 photoresist at 3000 rpm for 30 seconds.
5. Soft bake samples at 105°C for 2 minutes.
6. Cool down to room temperature.
7. Expose samples under UV light with 11.0 $mw/cm^2$ power density for 3.75 seconds without filter.
8. Develop samples in a Shipley MF312:$H_2O$ = 1:1.2 solution for 60 seconds.
9. Rinse samples thoroughly with D.I. water.
10. Blow dry gently with $N_2$.

# APPENDIX 6

# $O_2$ PLASMA ASHING

1. Turn on power supply and vacuum pump.
2. Vent and load samples into barrel asher.
3. Pump down the chamber and $O_2$ line below 50 µmHg.
4. Turn on $O_2$ valves and adjust flow rate until chamber pressure reaches 500 µmHg.
5. Turn on forward power to 100 watts and keep reflected power below 5 watts.
6. Run RF for 2 minutes.
7. When finished, vent and take out samples.
8. Turn off valves, $O_2$ gas, and power supply.

# APPENDIX 7

## REACTIVE ION ETCHING (RIE)

1. Turn on main power.
2. Vent and load samples into the chamber.
3. Turn on power switches of mechanical pump and high vacuum pump. (Not the valves)
4. Open roughing valve until chamber pressure drops below 7000 µmHg.
5. Close roughing valve.
6. Turn on high vacuum valve and blower switch.
7. Until chamber pressure drops to 20 µmHg or below, switch throttle valve to auto.
8. Turn on gases and adjust the flow rate. $CHF_3$ ~ 30 sccm, Argon ~ 3 sccm, and Helium ~ 7.5 sccm.
9. Wait until chamber pressure stabilized at 70 µmHg.
10. Turn on RF power. Adjust forward power to 350 watts and reflected power to 0 watt.
11. Start etching and timing.
12. After finished etching, turn off RF power, close gases, and switch throttle valve to open.
13. Wait for few minutes and turn off high vacuum valve and blower switch.
14. Vent and take out samples.
15. Turn off the mechanical pump and high vacuum pump.
16. Turn off main power.

# APPENDIX 8

# LAYOUT DIMENSION OF A POLARIZATION BEAM SPLITTER

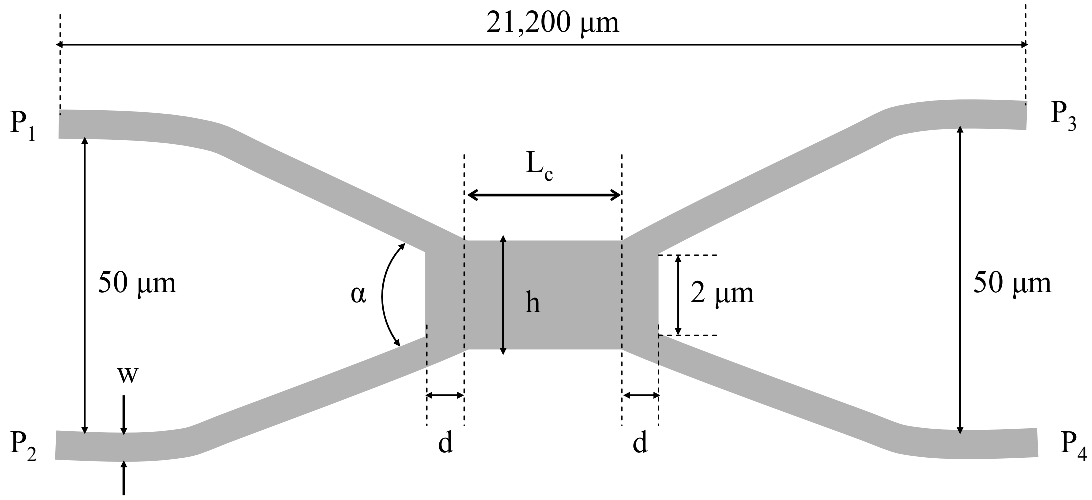

Figure 52. The mask layout of a polarization beam splitter.

Table 5. The dimension of a polarization beam splitter with α = 0.55° and d = 208 µm.

| Device # | 3C | 4C | 5C | 6C | 7C | 8C | 11C | 12C | 13C |
|---|---|---|---|---|---|---|---|---|---|
| w (µm) | 7 | 7 | 7 | 7 | 7 | 7 | 8 | 8 | 8 |
| $L_c$ (µm) | 200 | 220 | 230 | 240 | 260 | 280 | 210 | 230 | 250 |
| h (µm) | 14 | 14 | 14 | 14 | 14 | 14 | 16 | 16 | 16 |

# APPENDIX 9

## DEKTAK$^3$ SURFACE PROFILE MEASURING SYSTEM

1. Start the program.
2. Load a sample on the platform and turn on the light.
3. In program: SETUP→STYLUS→ALIGN, adjust the focus and alignment.
4. In program: SCAN PROGRAM→SCAN ROUTINE, set the scanning length and profile mode.
5. Select F4 key to start scanning.
6. Move R and M markers to proper position to level the scanned profile.
7. Move R and M markers again to right position to measure the thickness.
8. In program: ANALYSIS→ANALY FUNCTIONS→AVE HEIGHT→COMPUTE, the thickness is given.
9. After measurement, exit program and turn off the light.

# APPENDIX 10

# TITANIUM IN-DIFFUSION PROCESS

1. Load well cleaned samples on an alumina ($Al_2O_3$) D-tube, and put the D-tube in the center of an alumina long tube.
2. Use a glass rod to adjust the alumina tube to the center of a quartz tube of the furnace.
3. Seal the quartz tube with a quartz cap at front and connect to a bubbler.
4. Turn on compressed air valve and adjust air flow rate at the back of the furnace.
5. Adjust settings at front panel for desired diffusion temperature.
6. Wait until air flow rate stabilizes at 4 bubbles/second.
7. Turn on control switch.
8. Until current meters stabilize; turn on element switch.
9. It takes 45~60 minutes to heat up to the set temperature.
10. When current meters swing on/off, start counting diffusion time.
11. Frequently check the bubbling rate at front during diffusion.
12. Until reaching the total diffusion time, turn off the element and control switches right away.
13. Wait for 3~4 hours until the furnace temperature drops below 200°C.
14. Detach the bubbler. Then turn off compressed air valve.
15. Take out alumina tube and samples next day.

# APPENDIX 11

# POLISHING PROCESS

1. Apply one or two small drops of UV epoxy (Norland optical adhesive P/N 8101) on the clean waveguide surface of one sample.
2. Place the second sample with the waveguide surface faced down on top of the first sample.
3. Cure epoxy under UV light for 10 minutes each side.
4. Place samples into a polishing mount and secure the mount to a polish jig.
5. Start rough polishing with polish grit mixed in lapping oil.
6. Polish at 6 rpm speed for approximately 15~20 minutes.
7. Clean thoroughly the polishing mount and fixture before next step of fine polishing.
8. Mix 3μm diamond polishing grit with soap, water, and suspendex according to certain ratio.
9. Pour the mixed solution on the polishing plate and tray.
10. Turn on the pump for circulating the mixture.
11. Place the polishing jig on the plate gently, and very slowly increase the rotating speed of the plate to 16 rpm.
12. After polishing for one hour, inspect the end face with microscope. If not satisfied, do 20 minutes polishing interval and check again.
13. Clean all parts for finer polishing with the 0.3 μm diamond polishing grit.
14. Repeat the same procedure as polishing with 3 μm grit mixture.

15. Polish for 15~20 minutes at 16 rpm.
16. Take out samples and soak in MF312 until separate.
17. Clean the sample surface with methanol.
18. Inspect edge quality under microscope before optical testing.

# APPENDIX 12

# IMAGE REVERSAL PROCESS

1. Dehydrate samples at 135°C for 15 minutes.
2. Wait until samples cool down to room temperature.
3. Spin Clariant AZ 5214 photoresist at 3500 rpm for 30 seconds.
4. Pre soft-baked at 100°C for 1 minute.
5. Cool down for 5 minutes.
6. Fast exposed under 10.8 $mw/cm^2$ UV light for 1.25 seconds with a filter.
7. Second soft-baked at 110°C for 3 minutes.
8. Cool down for 10 minutes.
9. Flood exposed under 10.8 $mw/cm^2$ UV light for 1.75 minutes without a filter.
10. Develop samples in a Shipley MF312:$H_2O$ = 1:1.2 solution for 22 seconds.
11. Rinse samples well with D.I. water.
12. Blow dry samples gently with $N_2$.

# APPENDIX 13

## E-BEAM EVAPORATION PROCEDURE

1. Turn on the thickness monitor and the indicated light should flash twice. If light keeps flashing, the thickness crystal sensor needs to be replaced. Then turn it off.
2. Before venting the chamber, make sure the roughing valve and high vacuum valve are closed.
3. Vent the system.
4. Place crucibles with deposited materials and load samples.
5. Close the lid and turn on the mechanical pump and roughing valve to pump down the system.
6. Wait until the chamber pressure drops below 50 μmHg.
7. Close the roughing valve.
8. Turn on the high vacuum valve.
9. Turn off the mechanical pump.
10. Wait until system pressure is below $7 \times 10^{-6}$ torr.
11. Turn on the cooling system.
12. For $SiO_2$ deposition, start to heat up samples slowly until 360°C. Open the $O_2$ valve and adjust $O_2$ flow rate at 1 sccm when the sample temperature reaches 200°C. Keep the chamber pressure below $1.0 \times 10^{-5}$ torr.
13. Turn on the thickness monitor and set parameters of the density and z-ratio for deposited materials.

14. Start deposition.
15. For Cr/Au/Ti electrode deposition, wait for 15~20 minutes before depositing another metal layer.
16. After the deposition is complete, turn off the thickness monitor.
17. For deposited $SiO_2$ film, turn off the heating variac and open $O_2$ control knob all the way until the sample temperature drops below 50°C.
18. Leave the cooling system on for at least one hour.
19. Close the $O_2$ valve.
20. Turn off the cooling system.
21. Close the high vacuum valve.
22. Vent the system and take out samples.

# APPENDIX 14

## LAYOUT DIMENSION OF A TUNABLE ADD/DROP FILTER

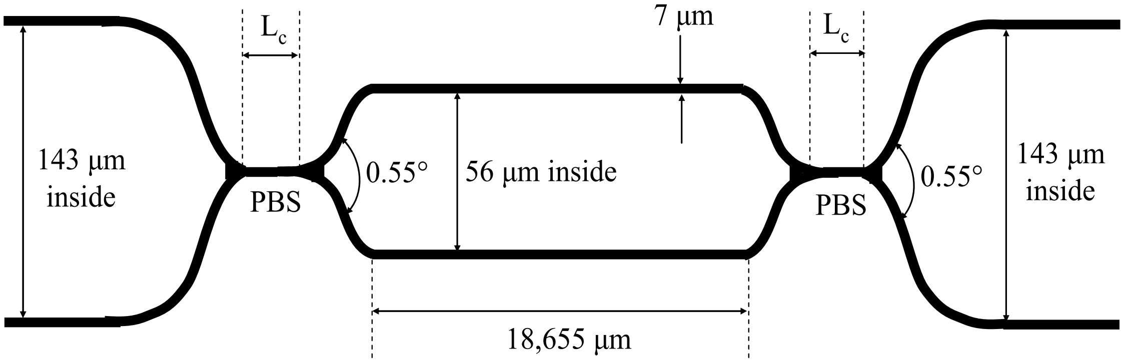

Figure 53. The waveguide layout diagram of a tunable add/drop filter.

Table 6. The mask layout of devices with different interaction length $L_c$ for tunable add/drop filters.

| Device # | 2C | 4C | 6C | 8C | 10C | 12C | 14C | 16C |
|---|---|---|---|---|---|---|---|---|
| $L_c$ (µm) | 240 | 260 | 280 | 300 | 240 | 260 | 280 | 300 |

# APPENDIX 15

# LAYOUT DIMENSION OF ELECTRODES

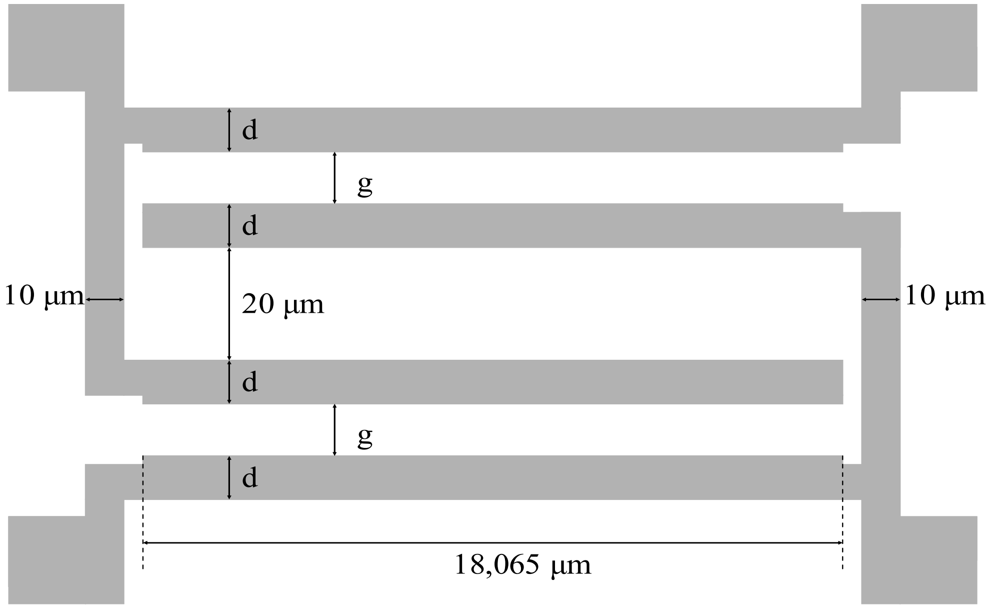

Figure 54. The layout of the electrode pattern.

Table 7. The layout dimension with different electrode gaps.

| Device # | 2C | 4C | 6C | 8C | 10C | 12C | 14C | 16C |
|---|---|---|---|---|---|---|---|---|
| d (μm) | 15 | 15 | 15 | 15 | 13 | 13 | 13 | 13 |
| g (μm) | 13 | 13 | 13 | 13 | 17 | 17 | 17 | 17 |

# APPENDIX 16

# FABRICATION PARAMETERS OF DEVICES

Table 8. Fabrication parameters of various devices.

| Device # | Ti Film Thickness (Å) | Diffusion Temperature (°C) | Diffusion Time (hours) |
|---|---|---|---|
| k106 | 1089 | 1025 | 9 |
| k77 | 1210 | 1050 | 12 |
| ks28 | 1327 | 1055 | 9 |
| ks29 | 1359 | 1055 | 9 |
| k211 | 1166 | 1035 | 11 |
| k209 | 1190 | 1050 | 11 |
| k208 | 1208 | 1050 | 11 |
| k210 | 1226 | 1050 | 11 |
| M6 | 1250 | 1060 | 10 |
| K17 | 1347 | 1055 | 9 |
| K11 | 1350 | 1055 | 9 |
| K14 | 1360 | 1055 | 9 |
| K13 | 1362 | 1055 | 9 |
| K10 | 1395 | 1055 | 9 |

# VITA

Hsin-Hui Kuo was born in Kaohsiung, Taiwan. She received her B.S. degree in electrical engineering from National Tsing Hua University, Taiwan in 1997. She attended Columbia University, New York, in Sept. 1997 and received her M.S. degree in electrical engineering in Dec. 1998. She started her doctoral program in electrical and computer engineering of Texas A&M University in Sept. 1999 and received her Ph.D. degree in May 2006. She can be reached at the following address:

Hsin-Hui Kuo
No. 41 Mong Li road, Neau Song Shiang,
Kaohsiung Shian, Taiwan